Integrating Fluoroscopy-derived Knee Kinematics Into Musculoskeletal Modelling to Investigate Knee Biomechanics

MSc Thesis

Susana Filipa Fonseca Fernandes

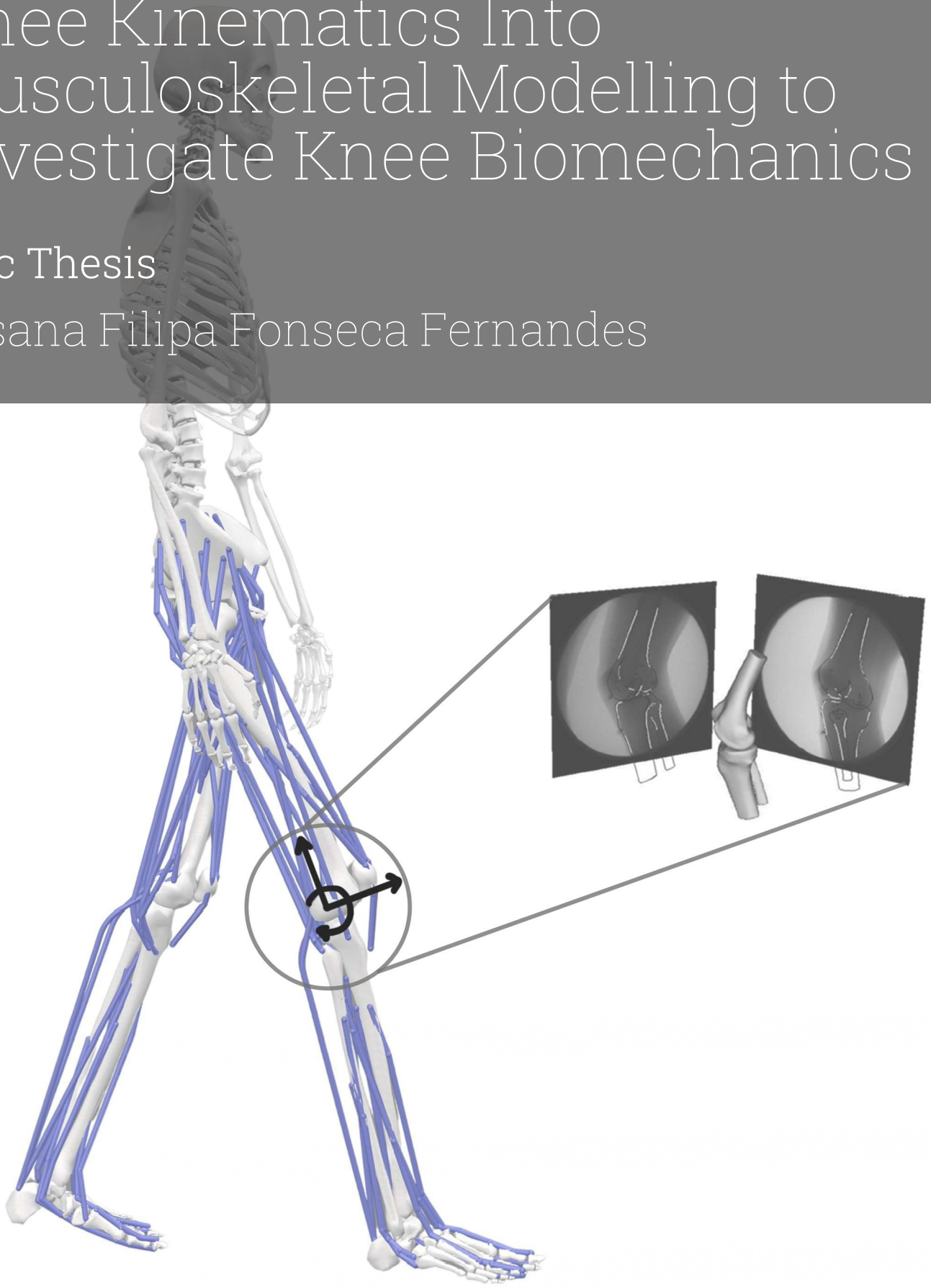

Integrating Fluoroscopy-derived Knee Kinematics Into Musculoskeletal Modelling to Investigate Knee Biomechanics

by

Susana Filipa Fonseca Fernandes

in partial fulfilment of the requirements of the Master of Science in Biomedical Engineering,
at the Delft University of Technology,
to be defended publicly on Thursday April 2, 2026, at 15:00.

Student number: 6085504

Thesis committee:	Prof. dr. ir. J. Harlaar,	TU Delft and Erasmus MC, supervisor and chair
	Drs. N. Dur,	Erasmus MC, daily supervisor
	S. Hörmann MSc,	TU Delft, supervisor
	Dr. ir. A. Seth	TU Delft, external committee member

Faculty: Faculty of Mechanical Engineering
Course code: BM51035

TU Delft

Preface

This thesis marks the end of my student years and the close of one of the most challenging chapters of this journey. From beginning my bachelor's at Instituto Superior Técnico to pursuing a master's at Delft University of Technology, I am deeply grateful for everything I have learned and for the ways I have grown along the way. Studying abroad was not always easy, but it has shaped me into the person I am today, and I have no doubt it was one of the best choices I have ever made.

I would like to thank my supervisors, Jaap Harlaar and Niels Dur, for their guidance and immense support throughout this project. To Sabrina Hörmann, thank you very much for all the hours you spent with me working through problems and trying to find solutions. I would also like to extend my gratitude to everyone in the Clinical Biomechanics group for their thoughtful ideas, encouragement, and sense of companionship.

On a more personal note, I am very grateful for the people around me. To all my friends, in Delft and back home, thank you for standing by me throughout all these years and for the memories we have made together. A special thank you goes to my family, who have supported me unconditionally, even in my somewhat unexpected and crazy idea of moving to another country. Your love and encouragement have meant more to me than you will ever know, and I miss you every single day. Finally, a very big thank you to Maarten for being my biggest support and for making everything brighter.

Susana Filipa Fonseca Fernandes
Delft, March 2026

Abstract

Introduction: Knee osteoarthritis (OA) is one of the most prevalent joint diseases worldwide, and mechanical loading plays an important role in its development and progression. Accurate knee joint kinematics are essential for computational models that estimate biomechanical parameters such as joint contact forces. Fluoroscopy enables accurate measurement of joint kinematics and may help overcome some limitations of conventional approaches, including soft tissue artefacts associated with optical motion capture and simplified model assumptions about knee joint motion.

Objective: This study aimed to develop and evaluate a modelling framework integrating fluoroscopy-derived knee kinematics into an existing musculoskeletal (MSK) model to assess whether this improves the prediction of tibiofemoral (TF) forces and medial–lateral load distribution, and how these outcomes are affected by different modelling choices.

Methods: Simulations were conducted using a generic MSK model and walking and squatting data from two subjects from the CAMS-knee dataset. TF flexion–extension (FE) rotations and anterior–posterior (AP) and superior–inferior (SI) translations were derived from fluoroscopy. FE rotation was prescribed during inverse kinematics (IK), while AP and SI translations were implemented as functions of FE rotation by replacing the model's original coordinate-coupling functions. Subject-specific mean kinematic relationships were also constructed for each activity. Different kinematic prescription configurations were evaluated. Joint loading was estimated using the rapid muscle redundancy (RMR) solver. Total TF forces, as well as medial and lateral compartment forces, medial force peaks, impulse, and medial load ratio (MLR), were evaluated against in vivo measurements.

Results: Fluoroscopy-derived kinematics showed larger excursions and distinct absolute magnitudes than the original model parametrisations. Their prescription led to changes in predicted TF forces and compartmental load distribution. For walking, the kinematic prescription had a limited influence on TF force predictions overall, although the FE-SI configuration showed the poorest agreement with in vivo data. For squatting, all configurations overestimated TF forces, but the FE-AP and FE-AP-SI configurations improved agreement with in vivo measurements. The FE-AP-SI configuration yielded the smallest total TF impulse differences relative to the in vivo reference in both subjects (1.663 BW·s and 0.377 BW·s), whereas FE and FE-SI produced the largest deviations. Lateral TF forces were predicted more accurately than total or medial forces. Subject-specific mean prescriptions yielded results nearly identical to trial-specific prescriptions.

Conclusions: The effect of prescribing fluoroscopy-derived knee kinematics in a generic MSK model depended on the activity and prescription configuration. No consistent improvements in walking were observed, whereas the FE-AP and FE-AP-SI configurations improved TF force predictions during squatting. Subject-specific mean prescriptions had a negligible effect on predicted forces, supporting a simplified implementation of the framework. Overall, this approach may improve the biomechanical fidelity of MSK models and advance understanding of knee joint loading.

Integrating Fluoroscopy-derived Knee Kinematics Into Musculoskeletal Modelling to Investigate Knee Biomechanics

1. Introduction

Osteoarthritis (OA) is a chronic, degenerative joint disease and the most prevalent joint disorder worldwide [1]. Particularly, the knee is among the most frequently affected joints because it is a complex structure that plays a significant role in load-bearing and mobility [2]. The estimated prevalence of knee OA is 22.9% in adults aged 40 years and older, and it is a major contributor to disability in older populations [3]. Moreover, the global burden of knee OA is expected to increase further with population ageing and rising obesity prevalence, as age and obesity are established risk factors for the disease [4,5].

From a pathophysiological perspective, knee OA is a multifactorial, progressive disease characterised by gradual degeneration of articular cartilage along with broader structural and biochemical changes in the joint. These include synovial inflammation, joint space narrowing, subchondral bone remodelling, osteophyte formation, and alterations in periarticular tissues, such as ligamentous laxity and weakening of the muscles surrounding the knee [6,7]. Collectively, these changes impair normal joint function and are commonly associated with pain, stiffness, and swelling. As the disease progresses, symptoms often lead to increasing functional limitations, reduced mobility, and further declines in muscle strength [8].

Mechanical loading is recognised as an important factor to both the onset and progression of knee OA [8]. Moderate, physiological joint loading is essential for maintaining articular cartilage integrity and function, as cartilage adapts to habitual loading patterns that support tissue homeostasis [9]. However, abnormal or excessive loading conditions can have detrimental effects. Specifically, altered knee joint kinematics, for example, due to injury or malalignment, can shift joint contact towards cartilage regions that typically experience low or infrequent loading, thereby increasing mechanical demand on less mechanically adapted tissue [10]. Elevated knee loading rates, as observed in high-impact physical activities and traumatic injuries, may also induce rapid increases in tissue stress that exceed the cartilage's capacity to tolerate load [11]. In addition, obesity is a major risk factor for the development of knee OA, as it contributes to excessive mechanical stress in the cartilage surface [12]. Together, these mechanical factors can disrupt the balance of cartilage metabolism and contribute to progressive joint deterioration [8,13].

A detailed understanding of knee joint mechanics and loading is essential for elucidating the biomechanical pathways underlying knee OA. Beyond mechanistic insight, this knowledge can inform the design of targeted interventions, such as gait retraining strategies, alignment-correcting procedures, and rehabilitation programmes aimed at reducing damaging joint loading [14]. Furthermore, accurate biomechanical characterisation can support implant design and clinical decision-making in areas such as surgical planning and postoperative evaluation [15].

Key biomechanical parameters of the knee joint include kinematics, contact forces, cartilage stress, and muscle or ligament forces, all of which are central to understanding its mechanical behaviour. Among these, joint contact forces, which are the compressive and shear forces exerted on the joint's articular surfaces, are important determinants of loading at this level and directly influence the mechanical environment experienced by the articular cartilage [15].

Although knee OA can involve both the medial and lateral tibiofemoral (TF) compartments, the medial compartment is affected more frequently [16,17]. Even in neutrally aligned knees, the medial compartment bears the majority of the TF compressive load during gait [18]. Moreover, individuals with knee OA often exhibit alterations in frontal-plane alignment. In particular, varus malalignment

shifts the mechanical axis medially and further increases medial compartment loading, a mechanism that has been associated with the development and progression of medial knee OA [17,19]. This further highlights the need to understand the role of knee joint mechanics in load distribution and in the resulting cartilage mechanical environment that may drive degeneration in knee OA.

A range of approaches has been employed to estimate the forces within the knee joint. One method is the use of instrumented knee implants, which enable accurate and direct in vivo measurement of TF contact forces and moments [20]. However, their use is restricted to post-arthroplasty populations and therefore cannot be readily generalised to native knees [21]. Another important source of insight into knee joint mechanics comes from ex vivo cadaveric studies [22,23], in which specimens are subjected to controlled loading using biomechanical testing systems that allow assessment of joint kinematics and contact mechanics [24]. However, the complexity of in vivo knee loading and motion is difficult to replicate experimentally, especially due to the absence of real muscle contractions, which limits the physiological relevance of these measurements [25]. Moreover, cadaveric models cannot capture biological processes central to OA, such as cartilage degeneration, tissue adaptation, and inflammation [24].

Computational modelling is widely used to evaluate knee joint mechanics, as it enables estimation of internal loading quantities that cannot be measured directly in vivo [26]. Within this framework, different modelling strategies are used depending on the mechanical quantities of interest. For instance, finite element models simulate tissue-level mechanics, such as cartilage stress, strain, and contact pressure, given the geometry, material properties, and boundary conditions [27]. Musculoskeletal (MSK) models are commonly applied to estimate knee joint forces. These models represent bones, musculotendon units, and joints as a mechanical system and typically rely on optimisation techniques to resolve muscle redundancy and estimate muscle and joint reaction forces. This is achieved by minimising a cost function, most commonly based on muscle activations. MSK models can also incorporate subject-specific anatomical parameters and, in some cases, electromyography (EMG) data to improve estimations [28]. Combinations of MSK and finite element models have been increasingly explored in recent years, as they offer complementary insights into knee joint biomechanics [29,30].

MSK models are typically driven by marker-based motion capture and force plate data, which provide marker trajectories and ground reaction forces (GRFs), respectively [31]. Marker trajectories are then used to derive whole-body kinematics, which define the model's motion. Accurate joint motion is therefore essential for obtaining reliable estimates of joint loading and contact mechanics [32].

However, marker-based motion capture is inherently limited by soft tissue artefacts because surface markers are placed on the skin over anatomical landmarks, and during dynamic tasks, the skin and soft tissues move relative to the underlying bones. This relative motion can introduce significant errors in the measured kinematics, which may propagate through the MSK simulations [33,34]. Displacements exceeding 15 mm at bony landmarks and up to 40 mm on the thigh have been reported [35]. In terms of knee joint angles, rotational errors can reach up to 9° during walking and as high as 24° during open-chain knee flexion [33]. This issue becomes even more relevant in overweight and obese subjects, due to the higher amount of adipose tissue [36].

In addition to these measurement-related limitations, inaccuracies may also arise from modelling assumptions, particularly in the representation of the knee joint. TF motion is described by six degrees of freedom (DoFs), including three rotations - flexion-extension (FE), varus-valgus (VV), and internal-external (IE) rotation - and three translations - medio-lateral (ML), anterior-posterior (AP), and superior-inferior (SI). Because this motion is mechanically complex, MSK models often simplify TF kinematics using generic relationships that prescribe translations and rotations as functions of knee flexion angle [37,38]. However, such formulations may not adequately reflect subject-specific behaviour or task-dependent variations in joint motion, thereby reducing the accuracy of the estimated TF contact forces.

To overcome these limitations, X-ray fluoroscopy has been increasingly used as a non-invasive imaging technique to accurately capture in vivo joint motion during dynamic, weight-bearing tasks [39]. By enabling direct visualisation of the underlying bone motion during movement, fluoroscopy substantially reduces kinematic errors caused by soft tissue artefacts in marker-based motion capture. Furthermore, it allows determining DoFs that are difficult to estimate reliably from marker-based motion capture alone. These data can therefore be used to inform MSK models with more realistic representations of TF motion.

It is important to note that fluoroscopy systems vary in configuration, each offering different levels of kinematic accuracy. Single-plane systems, which acquire images using a single X-ray source and detector, have reported in-plane accuracies of approximately 2.0 mm for translations and 1.5° for rotations, but exhibit larger errors in out-of-plane motion [40]. Biplane fluoroscopy uses two sources and detectors positioned at known angles and significantly improves accuracy, with values reported at 0.24 mm and 0.16° for translational and rotational measurements, respectively [32,41]. Additionally, high-speed fluoroscopy systems ($\geq$ 50 Hz [42]) enable the capture of rapid, high-impact dynamic movements.

Joint kinematics are obtained from fluoroscopy via 2D-3D model-based registration, in which the three-dimensional bone/implant models are aligned with the fluoroscopy images frame by frame to estimate the 6 DoF pose. Joint translations and rotations are then computed from the relative poses of the bones [32].

Some studies have already incorporated fluoroscopy-derived kinematics directly into MSK modelling workflows. For example, Nasab et al. [43] developed a total knee arthroplasty (TKA) model in which 6-DoF TF kinematics obtained from fluoroscopy were prescribed to fully define knee joint motion, rather than relying on marker-based knee kinematics. Similarly, Navacchia et al. [44] prescribed 6-DoF TF kinematics, together with in-plane patellofemoral (PF) joint motion, within a full-body MSK model. Overall, both studies highlight the value of incorporating in vivo fluoroscopy-derived kinematics into MSK workflows, since model outputs depend strongly on the assumed knee motion.

Following a different approach, Zheng et al. [35] incorporated fluoroscopy-derived TF kinematics by overwriting the knee joint kinematics obtained during the inverse kinematics (IK) step. In this framework, 5-DoF TF motions were directly replaced with fluoroscopic measurements, while SI translation was imposed as a flexion-dependent spline function derived from the fluoroscopy data. The authors reported improved accuracy of predicted joint loading relative to simulations driven solely by marker-based motion capture data, as evidenced by closer agreement with instrumented implant measurements. However, a potential limitation of this strategy is that overwriting knee kinematics after IK may disrupt global kinematic coherence across the full-body model, potentially introducing biomechanical inconsistencies in the resulting motion.

Gerus et al. [45] presented an approach that is particularly relevant to the present work. The authors developed a set of MSK models in which the knee joint was represented with five DoFs, with ML translation omitted, although they did not specify the rationale. VV and IE rotations were modelled as hinge joints. In contrast, knee FE was modelled as a planar joint, allowing knee flexion and sagittal-plane TF translations, namely AP and SI. These translational DoFs were defined as spline functions of the knee FE angle. The simulations were performed using experimental data from walking trials. To incorporate fluoroscopy-derived kinematics, the flexion-dependent spline relationships were adjusted to match the experimental data, thereby obtaining subject-specific in-plane translation behaviour. Notably, the authors concluded that incorporating subject-specific fluoroscopy-informed kinematics did not improve estimates of TF contact forces compared with models using generic spline functions, as evaluated against in vivo measurements.

Taken together, these selected studies illustrate several strategies for integrating fluoroscopy-derived knee kinematics into MSK models, ranging from directly prescribing TF motion to overwriting knee kinematics after IK, to adapting flexion-dependent spline parametrisations. However, the reported benefits are inconsistent, and the methodological choices and reporting practices vary sub-

stantially across studies (e.g., the point of integration in the workflow, the exact manner in which fluoroscopy data are imposed, and the validation metrics), making systematic comparison difficult and limiting reproducibility.

In this context, the objective of this study was to develop and evaluate a modelling framework that integrates fluoroscopy-derived knee kinematics into an existing MSK model to estimate knee joint reaction forces and medial–lateral load distribution, addressing the following research questions:

RQ1: Does the prescription of fluoroscopy-derived TF kinematics improve the predicted TF forces, compared with simulations driven solely by marker-based motion capture?

RQ2: How do distinct modelling choices, namely the prescription configurations and strategy, influence the estimated knee loading and the distribution of loads between the medial and lateral compartments during dynamic tasks?

The prescription configurations denote the selection of DoFs prescribed from fluoroscopy-derived kinematics, whereas strategy refers to whether these kinematics are defined on a trial-specific or subject-specific basis.

2. Methods

2.1. Musculoskeletal model

The generic OpenSim MSK model developed by Rajagopal et al. [37] was used in this study. This model includes 20 DoFs in the lower body and 17 in the torso and upper body, 80 lower-limb Hill-type musculotendon units (40 in each leg), and 17 torque actuators driving the upper body. The knee joint is defined as a 1-DoF joint, permitting only FE rotation, while the remaining DoFs (also called secondary DoFs) are parametrised as functions of this flexion angle. These parametrisations are based on the kinematic equations defined by Walker et al. [46]. Similarly, patellar kinematics were also parametrised as functions of the TF flexion angle, based on Arnold et al. [47]. The knee flexion angle was constrained to -10º to 120º.

The MSK model was scaled in the OpenSim GUI to match subject-specific anthropometry. Subsequently, an OpenSim-based analysis workflow was executed.

2.2. Dataset

This study utilised data from the Comprehensive Assessment of the Musculoskeletal System (CAMS) knee dataset [48]. This dataset comprises kinematic and kinetic testing data acquired from six subjects (5 males, 1 female; age 75 $\pm$ 5 years; body mass 89 $\pm$ 13 kg; height 172 $\pm$ 4 cm), each implanted with an instrumented TKA. The implant, an ultra-congruent INNEX FIXUC (Zimmer Biomet, Switzerland), integrates strain gauges and a telemetry transmitter to enable in vivo measurement of all six components of TF joint contact forces and moments, with a reported mean measurement error below 2% at a sampling frequency of 90-100 Hz [49].

The dataset also includes subject information, such as anthropometric and anatomical data, subject-specific implantation data, and trial data and videos from multiple activities, including walking and squatting. Trial data include skin-marker trajectories acquired via optical motion capture at 100 Hz for whole-body kinematics, and GRF measurements obtained from force plates at 2000 Hz. The GRF data provided in the dataset were corrected, following the calibration procedure described by List et al. [50], to improve centre of pressure (CoP) estimation. In addition, lower-limb EMG data were collected using a 16-channel system with wireless telemetry communication, also at 2000 Hz.

A moving single-plane fluoroscopy system operating at 25 Hz was used to acquire sagittal-plane images throughout the activities [50]. For each frame, the three-dimensional models of the implant components were registered to the fluoroscopic images using the method described by Burckhardt et al. [51]. The reported accuracy for this registration procedure indicated errors of less than 1º for all rotational components, less than 1 mm for in-plane translations, and less than 3 mm for out-of-plane translations. The transformation matrices resulting from the registration procedure were reported in

the dataset and correspond to the absolute poses of the femoral and tibial implant components in the laboratory reference frame, at each time frame.

All measurements were recorded simultaneously and temporally synchronised, and the integrated dataset was reported based on the highest sampling frequency of 2000 Hz. Gait cycles were defined based on a 25 N vertical GRF threshold, and the heel-strike and toe-off events were reported in the dataset.

In this dataset, multiple coordinate systems are defined to express the measured quantities, which are highly relevant to subsequent steps that integrate data from different measurement modalities. These are detailed in Appendix A.

2.3. Data processing

Motion capture marker trajectories were extracted from the dataset and expressed in the global reference frame of the MSK modelling environment. Gaps were filled by interpolation, after which the data were low-pass filtered using a 4th-order Butterworth filter with a cut-off frequency of 6 Hz. GRFs were similarly extracted from the dataset, expressed in the appropriate reference frame, and filtered using the same filter.

Fluoroscopy data required additional processing to reconstruct the TF kinematics. The 6-DoF TF kinematics were obtained by computing the relative pose of the tibial component with respect to the femoral component at each time frame from the absolute implant poses reported in the dataset. These kinematics were first obtained in the dataset-specific implant-based coordinate system (CS_{JWI}; see Appendix A), and then transformed to the knee joint reference frames of the MSK model, by positioning the implant components on the scaled model according to subject-specific implantation data, and extracting the adequate transformation matrices (details of this approach are in Appendix B). The reconstructed in-plane kinematics were subsequently filtered using the same low-pass filter applied to the marker and GRF data.

EMG data were processed following the approach described by Nejad et al. [52]. The raw EMG signals were first bandpass filtered using a 4th-order Butterworth filter with lower and upper cut-off frequencies of 10 and 300 Hz, respectively. The signals were then offset-corrected, rectified, and smoothed using a moving average filter with a 0.25 s window. For each muscle, the resulting signal was normalised to the maximum activation recorded across all trials for both activities and both subjects.

2.4. Prescription of fluoroscopy-derived TF kinematics

Fluoroscopy-derived TF kinematics were incorporated into the MSK model through coordinate prescription. Due to the monoplanar imaging configuration, only the in-plane DoFs, namely the AP and SI translations, and the FE rotation were considered, as the out-of-plane DoFs are subject to greater measurement inaccuracies.

As described previously, FE rotation is the only independent coordinate of the TF joint, whereas the remaining DoFs are kinematically coupled and prescribed as functions of this coordinate. Consequently, fluoroscopy-derived FE rotations were directly prescribed during the IK step by defining a coordinate tracking task that followed the measured trajectory. In contrast, the in-plane translations required direct overwriting of the coordinate-coupling functions in the model definition.

From the fluoroscopy data, the three in-plane DoFs were extracted for each time frame. For each gait cycle and each squat trial, the fluoroscopy-derived AP and SI translations were paired with the corresponding FE values, and cubic polynomial functions were fitted to describe these translations as continuous functions of FE rotation for both activities. The resulting relationships were implemented as spline-based coupling functions that replaced the original model definitions. This enabled gait cycle-specific prescription for walking, and trial-specific prescription for squatting, of TF AP and SI translations.

In addition, subject-specific mean relationships were obtained by averaging the fitted AP–FE and SI–FE relationships across gait cycles for walking and across squat trials for squatting. For each

activity, a common FE domain spanning the full observed flexion range was defined to ensure stable spline behaviour during simulation. These mean relationships were also implemented as spline-based coupling functions to allow comparison between cycle-specific and averaged kinematic prescriptions for walking, and between trial-specific and averaged prescriptions for squatting.

Representative examples of the curve fitting to the experimental data and the resulting subject-specific average relationships are provided in Appendix C. Additionally, the comparison of the spline-based AP and SI translations with the original model parametrisations is also presented.

2.5. Simulations

Simulations were conducted in OpenSim using data from two subjects (K5R and K8L), selected from the dataset based on measurement quality. Only walking and squatting activities were included. For each subject, the scaled MSK model was employed, and simulations were executed using a sequential analysis workflow.

IK was first applied to determine the model's generalised coordinates (joint angles and translations) by tracking experimental marker trajectories. This step is formulated as a weighted least squares problem, in which the sum of squared marker and coordinate tracking errors is minimised. Higher weights were assigned to markers located on bony landmarks, such that the solution prioritised accurate tracking of anatomically meaningful marker locations. Based on the IK outputs, muscle moment arms about the knee joint were computed for all muscles across the entire duration of each trial. Subsequently, inverse dynamics (ID) was performed using the computed kinematics and external load data (GRFs) to determine the net joint moments and forces consistent with the observed motion.

In this project, muscle activations and joint contact forces were estimated using a rapid muscle redundancy (RMR) solver [53]. This algorithm takes the joint trajectories obtained from IK (coordinate values, velocities and accelerations), together with the experimental GRFs, and solves the muscle redundancy problem via numerical optimisation. Specifically, at each time instant, it minimises the sum of weighted squared muscle activations, while enforcing physiological constraints and dynamic activation behaviour. Further details on the cost function of the RMR solver are provided in Appendix D.

Additionally, in this algorithm, muscle force generation includes active and passive fibre contributions, which are length- and velocity-dependent. The optimisation is constrained to ensure dynamic consistency, such that the model-predicted generalised accelerations match those derived from the kinematic input at each time step. Physiologically plausible muscle activation dynamics are further enforced, with muscle activations bounded at each time step based on the activation in the previous step and the time-step size. Finally, joint reaction forces are evaluated efficiently within the RMR formulation by expressing them as linear functions of the estimated muscle activations.

A series of simulation configurations was performed to evaluate the effects of prescribing fluoroscopy-derived TF kinematics. First, simulations with no prescribed fluoroscopy-based DoFs were conducted, relying solely on marker-driven kinematics. Subsequently, TF kinematics were selectively prescribed for each gait cycle/squat trial. FE rotation was prescribed during the IK step in all configurations, as it represents the independent DoF of the joint and forms the basis for the coupled translational relationships.

Four prescription combinations were implemented: FE only (FE), FE combined with AP translation (FE-AP), FE combined with SI translation (FE-SI), and FE combined with both AP and SI translations (FE-AP-SI). Each configuration was executed independently for every gait cycle/squat trial, while maintaining identical model and solver settings.

Additionally, to evaluate different kinematic prescription strategies, simulations using subject-level mean relationships were performed and compared with those based on relationships derived for each gait cycle/squat trial. In these simulations, the FE trajectory remained specific to the simulated gait cycle/squat trial, while the AP and/or SI translations were replaced by subject-specific AP-FE and SI-FE mean relationships. Three configurations were tested: FE with mean AP translation (FE-AP-average), FE with mean SI translation (FE-SI-average), and FE with both mean AP and mean SI

translations (FE-AP-SI-average). Thus, FE remained specific to each simulated motion, whereas AP and/or SI translations were prescribed at the subject level.

2.6. Data analysis

The RMR solver yields the joint forces and moments at each time step, muscle activations, and actuator (including reserves) forces. Joint forces were analysed to assess the effects of prescribing fluoroscopy-derived TF kinematics. At each time step, the total compressive TF force was extracted. Medial and lateral compartment loading were estimated, following the approach described by Kutzner et al. [54]. Specifically, the medial contact force was computed as

$$F_{med} = \frac{|F_y|}{2} - \frac{|M_x|}{l} \tag{1}$$

where l is the distance between the medial and lateral condyles, F_y is the axial (compressive) TF force component, and M_x is the moment generated by this axial force acting on the tibia with a medial-lateral lever arm (adduction moment). The distance between the medial and lateral condyles was estimated as half the distance between the medial and lateral epicondyle surface markers in the static pose. Experimental validation showed that the medial TF force can be estimated with an error below 3% when $|F_y| > 1000$ N [55]. Therefore, for the walking simulations, compartmental force estimation was performed only during the stance phase. For the squatting simulations, compartmental forces were evaluated over the full analysed trial duration. The lateral compartment force was calculated as $F_{lat} = |F_y| - F_{med}$.

For the walking trials, outcome metrics were extracted from the estimated F_{med} for each gait cycle and simulation configuration. Specifically, the first and second stance-phase peaks of this force component, as well as its impulse, computed as the time integral over stance, $\int_{stance} F_{med}(t)\,dt$, were determined. For each metric, the difference between the simulated and the corresponding in vivo values, measured by the instrumented implants, was calculated. These differences were summarised per simulation configuration, and reported as the median and interquartile range (IQR).

For the squatting trials, the impulse of the total TF force was computed as $\int_{squat} F_{total}(t)\,dt$ and likewise reported as the median and IQR of the difference relative to the in vivo measurements. In addition, the medial load ratio was calculated for both tasks as $MLR(t) = F_{med}(t)/|F_y(t)|$, to quantify the fraction of the axial load transmitted through the medial compartment.

For the walking trials, force-related outputs were time-normalised to 0–100% of the stance phase, whereas kinematics and muscle-related outputs were time-normalised to 0–100% of the gait cycle. For the squatting trials, all results were time-normalised to 0–100% of the squat cycle. All force components were additionally normalised to body weight (BW).

2.7. Statistical analysis

Statistical parametric mapping (SPM) was used as the primary statistical analysis method in this study. SPM enables statistical evaluation of continuous waveform data across the full domain of interest, rather than at discrete time points, and is therefore well suited for biomechanical data [56].

One-dimensional SPM was used to assess differences of the estimated against the in vivo TF loading profiles over the analysed interval, corresponding to the stance phase for walking and the full analysed interval for squatting. Statistical comparisons were performed using non-parametric paired t-tests with a significance level of $\alpha = 0.05$. A non-parametric approach was adopted due to the small number of curves per configuration. This analysis was conducted for the total, medial and lateral TF force curves by comparing each predicted force with the corresponding in vivo measurement. For each prescription configuration, the proportion of the analysed interval showing statistically significant differences was extracted. In addition, the root-mean-squared error (RMSE) was computed over these significant regions to quantify the magnitude of the deviation where the curves differed significantly. The same SPM analysis was subsequently performed to assess differences between the predicted and in vivo-derived MLR curves.

3. Results

3.1. Walking simulations

All curves shown in this section represent the mean across the simulated gait cycles, with the corresponding standard deviation (± 1 SD) indicated by the shaded regions. Six gait cycles ($n = 6$) were simulated for each subject and prescription configuration.

3.1.1. Knee kinematics

Figure 1 shows the in-plane TF kinematics obtained from the IK step during the walking trials for subject K5R under each prescription configuration.

The graph demonstrates that the model closely follows the prescribed kinematics, as expected. The FE rotation obtained from fluoroscopy is very similar to that derived from motion capture, whereas larger differences were observed for the translational DoFs. For both AP and SI translations, the overall curve shape remained comparable to that defined by the original model relationships, but the range and the absolute magnitude varied considerably. Similar trends were observed for subject K8L, but with larger translational excursions and smaller standard deviations across cycles, indicating more homogeneous kinematics (see Appendix E).

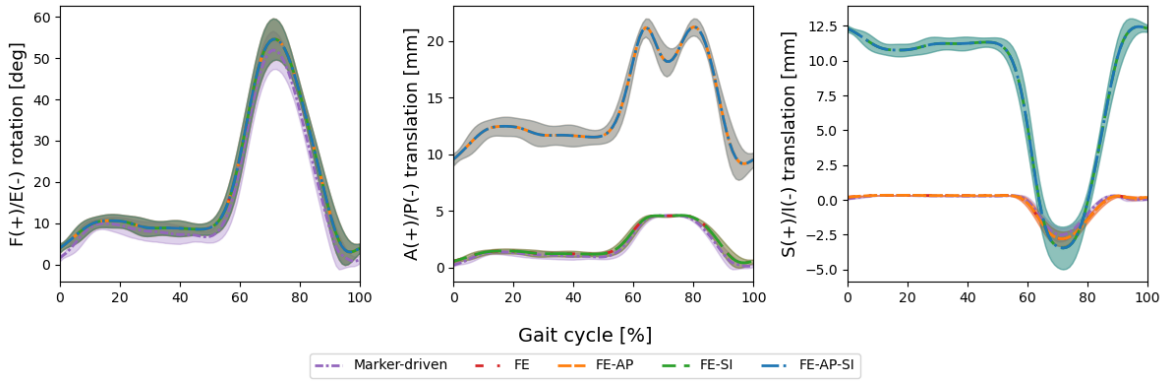

Figure 1. In-plane TF kinematics across the gait cycle for subject K5R under each prescription configuration.

3.1.2. Total TF force estimations

Figure 2 shows the estimated total TF compressive force during the walking trials for each prescription configuration for subjects K5R (a) and K8L (b). Table 1 summarises the statistical comparison between the estimated and in vivo total TF force profiles obtained for walking in both subjects across all prescription configurations.

Overall, the predicted total TF force curves for subject K5R (Figure 2 (a)) reproduced the characteristic double-peaked pattern associated with the stance phase of gait, with most prescription configurations yielding curves that followed the in vivo data well in terms of shape. The statistical analysis further confirms the model's overall good performance across all prescription configurations, with significant differences limited to small portions of the stance phase.

Notably, among the tested configurations, the FE-SI configuration showed the largest deviation from the in vivo forces. In this case, the predicted curve diverged from in vivo data throughout mid- and late stance and exhibited an unexpectedly high peak not observed in the other configurations. This is also reflected in the highest RMSE value (0.624 BW) and the largest proportion of stance phase showing significant differences (9.7%). In contrast, FE-AP demonstrated the best overall agreement with the in vivo data, with no statistically significant differences detected across the stance phase.

The FE and marker-driven prescription configurations also performed well, yielding nearly identical results with comparable RMSE values (≈ 0.21 BW) and only minimal regions of significant difference. The FE-AP-SI configuration, corresponding to the most constrained model, showed intermediate performance, with more deviations from the in vivo curve.

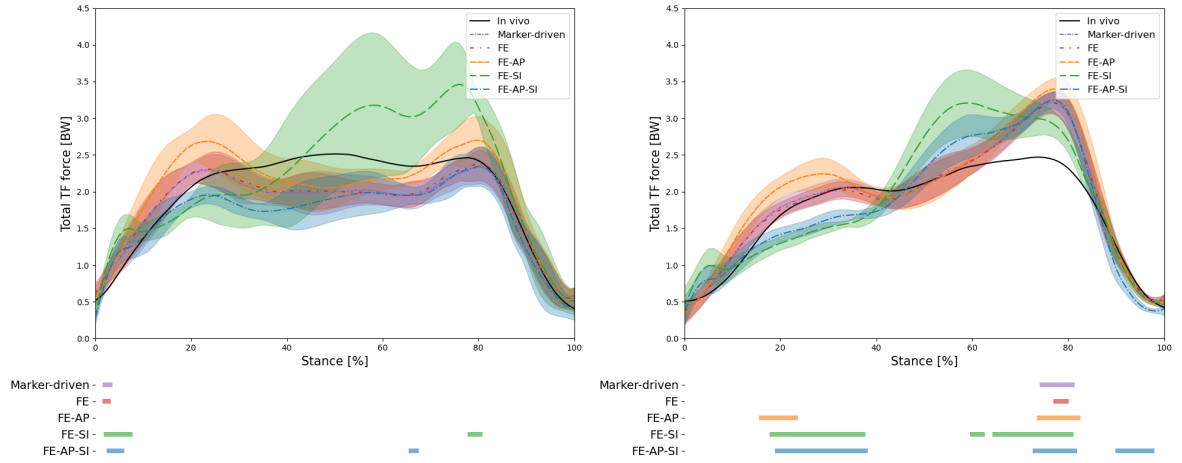

(**a**) (**b**)

Figure 2. Estimated total TF compressive force across the stance phase of gait for subjects K5R (**a**) and K8L (**b**) under each prescription configuration. The panels below each plot indicate regions of statistically significant differences between each configuration and the in vivo measurements.

	Subject K5R		***Subject K8L***	
Configuration	**Total TF force**		**Total TF force**	
	% Sig	**RMSE**	**% Sig**	**RMSE**
Marker-driven	2.0	0.211	7.1	0.787
FE	1.7	0.212	3.1	0.810
FE-AP	0.0	-	17.1	0.747
FE-SI	9.7	0.624	39.5	0.556
FE-AP-SI	5.7	0.321	36.3	0.486

Table 1. Statistical comparison of estimated total TF forces against in vivo measurements across the stance phase of gait for subjects K5R and K8L under each prescription configuration. Reported metrics are the percentage of the stance phase with statistically significant differences (% Sig) and the RMSE (in BW) computed over those significant regions. Where no statistically significant differences were found, RMSE is not applicable (-).

For subject K8L (Figure 2 (b)), the model predictions revealed substantially larger deviations from the in vivo force measurements. In particular, the second peak of the stance phase was consistently overestimated across all configurations. As observed for K5R, the marker-driven and FE configurations produced almost identical results, reproducing the first peak well but markedly overestimating the second peak, which resulted in relatively larger RMSE values (0.787 and 0.810 BW, respectively).

The FE-AP configuration, which demonstrated the best performance for subject K5R, performed less well for K8L, considerably overestimating both peaks and showing significant differences in 17% of the stance phase. The FE-SI and FE-AP-SI configurations exhibited the worst performance, with statistically significant differences exceeding 35% of the stance phase for both. Unlike the other configurations, these configurations also underestimated the first peak, indicating a more pronounced mismatch in the predicted loading pattern.

3.1.3. Medial and lateral TF force estimations

Figures 3 and 4 depict the estimated medial and lateral TF forces during the walking trials for each prescription configuration for subjects K5R and K8L, respectively. Table 2 summarises the statistical comparison between the estimated and in vivo medial and lateral TF force profiles across all configurations for both subjects. In addition, tables 3 and 4 report the differences in the medial TF force peaks and impulse relative to the in vivo measurements for subjects K5R and K8L, respectively.

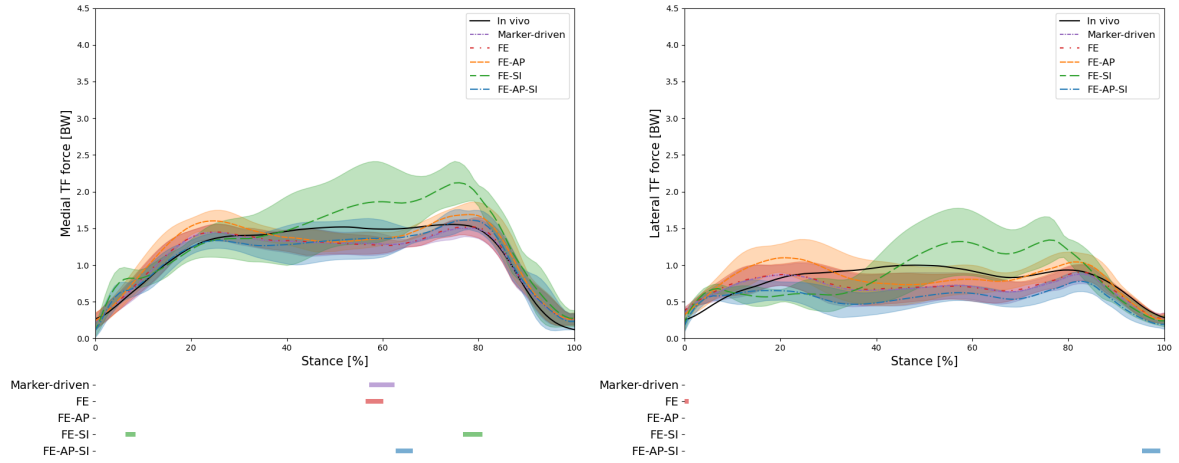

(**a**) (**b**)

Figure 3. Estimated medial (**a**) and lateral (**b**) TF force across the stance phase of gait for subject K5R under each prescription configuration. The panels below each plot indicate regions of statistically significant differences between each configuration and the in vivo measurements.

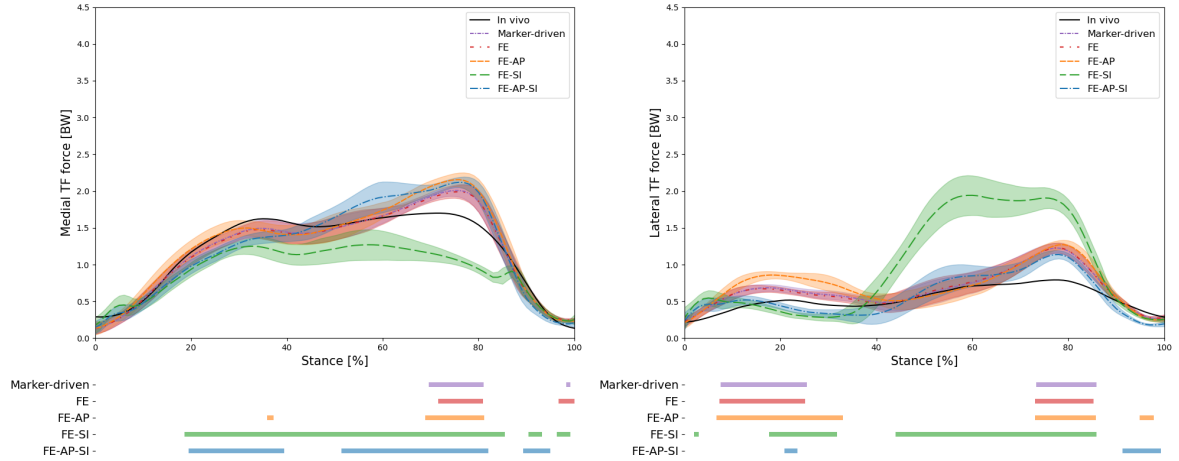

(**a**) (**b**)

Figure 4. Estimated medial (**a**) and lateral (**b**) TF force across the stance phase of gait for subject K8L under each prescription configuration. The panels below each plot indicate regions of statistically significant differences between each configuration and the in vivo measurements.

	Subject K5R				*Subject K8L*			
Configuration	**Medial TF force**		**Lateral TF force**		**Medial TF force**		**Lateral TF force**	
	% Sig	**RMSE**	**% Sig**	**RMSE**	**% Sig**	**RMSE**	**% Sig**	**RMSE**
Marker-driven	5.4	0.212	0.0	-	12.2	0.313	30.1	0.297
FE	3.6	0.229	0.9	0.135	12.5	0.287	29.6	0.294
FE-AP	0.0	-	0.0	-	13.7	0.444	41.6	0.360
FE-SI	6.1	0.462	0.0	-	71.9	0.410	56.5	0.915
FE-AP-SI	3.5	0.126	3.8	0.160	55.8	0.294	10.7	0.148

Table 2. Statistical comparison of estimated medial and lateral TF forces against in vivo measurements across the stance phase of gait for subjects K5R and K8L under each prescription configuration. Reported metrics are the percentage of the stance phase with statistically significant differences (% Sig) and the RMSE (in BW) computed over those significant regions. Where no statistically significant differences were found, RMSE is not applicable (–)

Configuration	Δ Peak 1		Δ Peak 2		Δ Impulse	
	Median	IQR	Median	IQR	Median	IQR
Marker-driven	-0.069	0.077	0.008	0.189	-0.060	0.104
FE	-0.074	0.076	0.003	0.097	-0.050	0.077
FE-AP	0.073	0.041	0.130	0.149	0.034	0.061
FE-SI	0.135	0.495	0.581	0.224	0.215	0.203
FE-AP-SI	-0.152	0.193	0.076	0.231	-0.052	0.115

Table 3. Differences in medial TF force first peak (Δ Peak 1), second peak (Δ Peak 2), and impulse (Δ Impulse) relative to in vivo measurements for subject K5R under each prescription configuration, reported as the median and IQR across all simulated gait cycles. Peaks are expressed in BW and impulse BW·s.

Configuration	Δ Peak 1		Δ Peak 2		Δ Impulse	
	Median	IQR	Median	IQR	Median	IQR
Marker-driven	-0.148	0.081	0.310	0.210	-0.020	0.101
FE	-0.161	0.095	0.289	0.231	-0.026	0.103
FE-AP	-0.110	0.075	0.451	0.232	0.025	0.093
FE-SI	-0.355	0.089	-0.433	0.126	-0.259	0.028
FE-AP-SI	-0.239	0.000*	0.424	0.199	-0.006	0.073

Table 4. Differences in medial TF force first peak (Δ Peak 1), second peak (Δ Peak 2), and impulse (Δ Impulse) relative to in vivo measurements for subject K8L under each prescription configuration, reported as the median and IQR across all simulated gait cycles. Peaks are expressed in BW and impulse BW·s. * IQR = 0 because only one curve exhibited a detectable first peak.

The medial and lateral TF force curves provide further insight into the effect of the prescribed kinematics. For subject K5R (Figure 3), the medial TF force curves generally showed close agreement with the in vivo measurements. As observed previously, the FE-SI configuration showed the largest deviation from the in vivo data, which was also reflected in the higher percentage of stance with significant differences, and in the medial force metrics, particularly in the median differences in the second peak (Δ Peak 2 = 0.581 BW) and impulse (Δ Impulse = 0.215 BW·s).

Once again, the FE-AP configuration showed the best overall agreement, with no statistically significant differences detected for either the medial or lateral force components. The FE and marker-driven configurations produced very similar results, whereas FE-AP-SI showed intermediate performance, with somewhat larger deviations in the medial force metrics. Interestingly, regarding the lateral TF force, the FE-SI, FE-AP and marker-driven configurations all showed 0% significant differences relative to the in vivo data.

The graphs presented for K8L (Figure 4) highlight the differences in performance across prescription configurations for this subject. The FE-SI configuration stands out most prominently, exhibiting a marked underestimation of the medial force alongside a substantial overestimation of the lateral component. This behaviour across compartments resulted in statistically significant differences from in vivo measurements across more than 70% of the stance phase for the medial force, and more than 55% for the lateral, with the latter yielding an RMSE of approximately 0.9 BW. The medial loading metrics further support these observations, showing pronounced underestimations of the first peak and impulse of the medial TF force.

Among the remaining configurations, FE and marker-driven again showed very similar behaviour, as observed for the first subject, with statistically significant differences mainly concentrated in late stance and with medial loading metrics remaining close to each other. In addition to overestimating the second peak of the medial TF force, the FE-AP configuration also significantly overestimated the lateral TF force. The FE-AP-SI configuration showed widespread significant differences in the medial component, exceeding 55% of the stance phase, although the difference in medial force impulse relative to the in vivo measurements remains small.

3.1.4. Load distribution

The MLR further illustrates how the different prescription strategies influence load distribution between the knee compartments. Figure 5 depicts the estimated MLR during the walking trials across prescription configurations, for both subjects analysed.

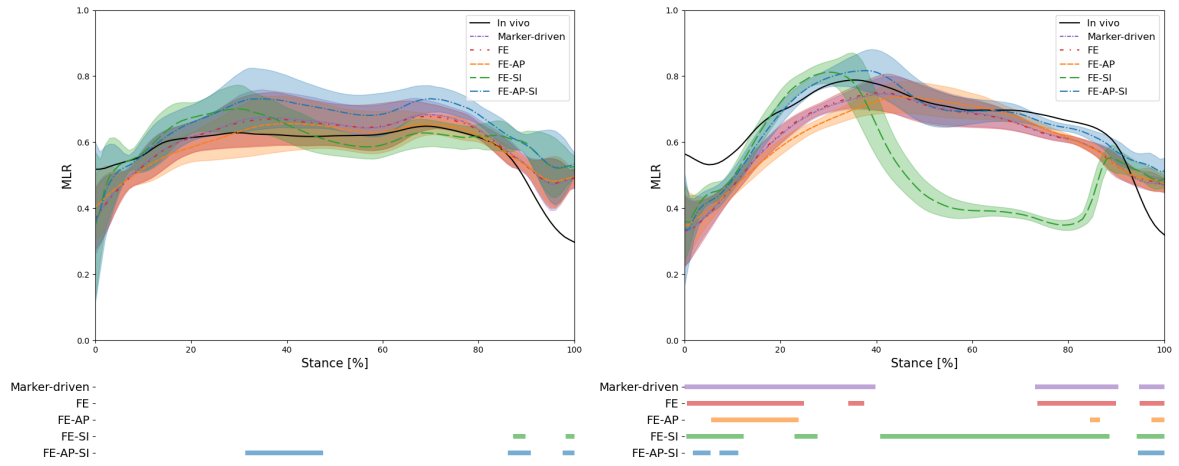

(**a**) (**b**)

Figure 5. Estimated MLR across the stance phase of gait for subjects K5R (**a**) and K8L (**b**) under each prescription configuration.

At the beginning and end of stance, the predicted MLR deviates from the in vivo estimations for both subjects across all prescription configurations. In particular, during late stance (85–100%), none of the models reproduced the decline in MLR observed in vivo for either subject.

For K5R (Figure 5 (a)), during most of the stance phase, FE, FE-AP, and marker-driven configurations remained close to the in vivo MLR, consistent with their good agreement in both medial and lateral TF force components. In contrast, the FE-AP-SI configuration showed the largest and most sustained overestimation of the MLR throughout mid-stance.

The FE-SI configuration behaves differently from all other prescriptions, being the only configuration to reduce the MLR during part of the stance, indicating a shift in load distribution toward the lateral compartment. This is consistent with the elevated lateral TF force observed for this configuration in Figure 3 (b), where it diverged from all others.

As for K8L (Figure 5 (b)), the FE-SI configuration yielded by far the largest deviations from the in vivo MLR, with a pronounced drop in the ratio throughout the stance phase. This behaviour likely reflected a substantial and non-physiological shift in loading from the medial to the lateral compartment, a pattern not observed in any of the other configurations. The remaining configurations exhibited broadly similar trends for most of the stance phase, following the overall shape of the in vivo MLR curve, although statistically significant differences are present across several regions of the stance phase. Notably, and in contrast to subject K5R, the FE-AP-SI configuration showed the closest agreement with the in vivo MLR, among all prescription strategies, for this subject.

3.1.5. Kinematic prescription strategy

Figure 6 presents a representative comparison between gait cycle-specific and subject-level mean prescriptions for the FE-AP-SI configuration during the walking trials for subject K5R.

The predicted total, medial, and lateral TF force curves for the cycle-specific and subject-level mean prescriptions overlapped almost entirely, indicating that averaging the kinematic relationships at the subject level had a negligible effect on the estimated TF forces. As this was also observed for the FE-AP and FE-SI configurations, only the FE-AP-SI configuration is presented. Comparable results were obtained for subject K8L and are provided in Appendix F.

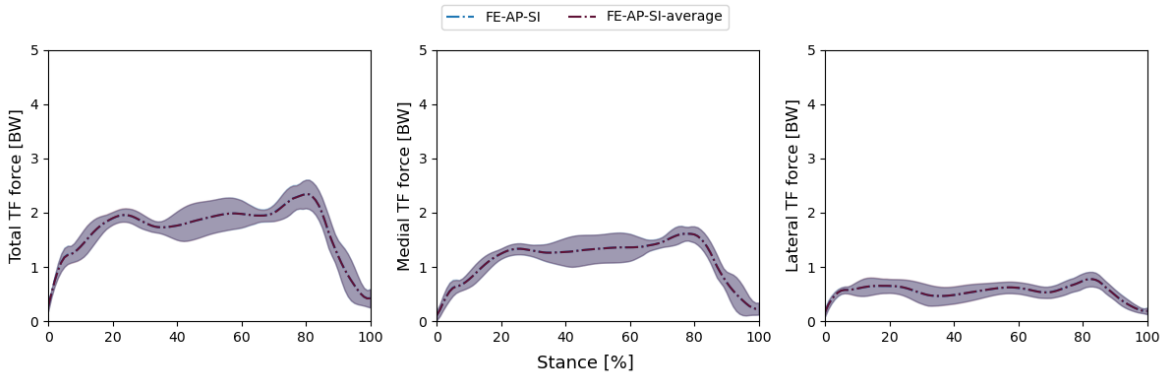

Figure 6. Comparison of gait cycle–specific and subject-level mean prescriptions for the FE-AP-SI configuration during walking for subject K5R. Estimated total, medial, and lateral TF forces across the stance phase of gait are shown for both approaches.

3.2. Squatting simulations

All curves shown in this section represent the mean across the simulated squatting trials, with the corresponding standard deviation (± 1 SD) indicated by the shaded regions. Five complete squats ($n = 5$) were simulated for each subject and prescription configuration.

3.2.1. Knee kinematics

Figure 7 shows the in-plane TF kinematics obtained from the IK step during the squatting trials for subject K5R and for each prescription configuration.

As in the walking simulations, the model closely follows the prescribed kinematics. During squatting, the fluoroscopy-derived FE rotation showed a higher peak around mid-squat than the FE rotation obtained from the simulations driven solely by marker data. The main differences were again observed for the AP and SI translations, particularly in their excursion and absolute magnitude. Similar trends were observed for subject K8L, although with larger translational excursions and smaller standard deviations across cycles, which indicates more homogeneous kinematics (see Appendix E).

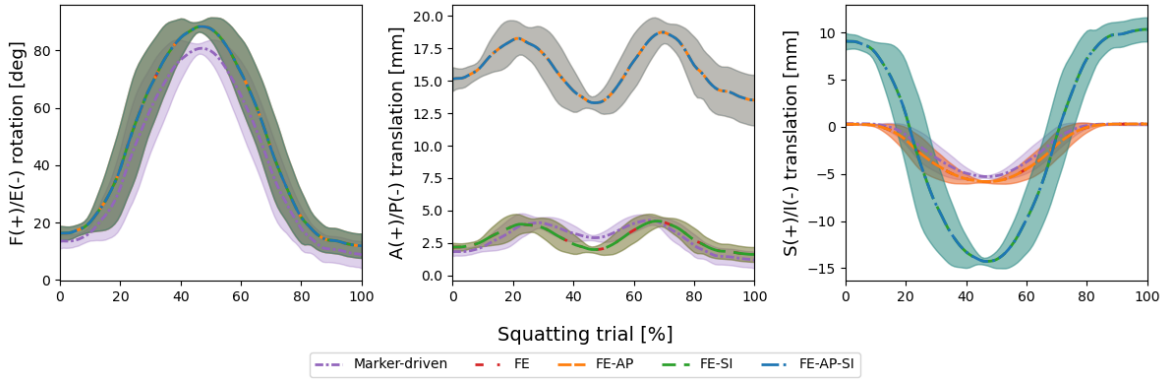

Figure 7. In-plane TF kinematics during squatting for subject K5R under each prescription configuration.

3.2.2. Total TF force estimations

For the squatting trials, Figure 8 shows the estimated total TF compressive force for subjects K5R (**a**) and K8L (**b**) under each prescription configuration. The corresponding statistical comparison between the estimated and in vivo total TF force profiles for both subjects is reported in Table 5. Additionally, Table 6 depicts the differences in the total TF force impulse relative to the in vivo measurements for both subjects.

For this task, the model consistently and substantially overestimated the total TF force across all prescription configurations, especially in the deep flexion region (30-70% of the task). This trend was observed for both subjects, although subject K8L generally exhibited larger discrepancies relative to

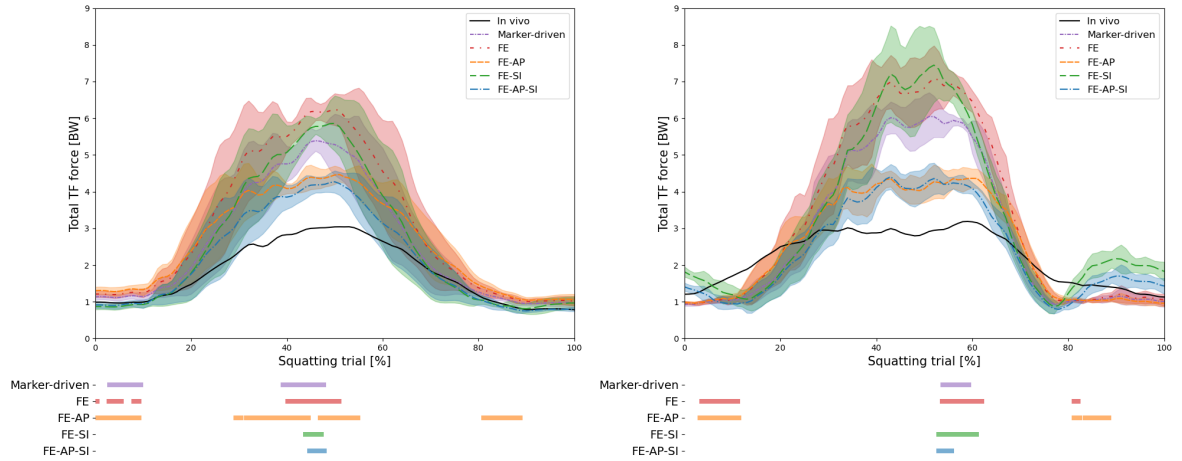

(**a**) (**b**)

Figure 8. Estimated total TF compressive force during squatting for subjects K5R (**a**) and K8L (**b**) under each prescription configuration. The panels below each plot indicate regions of statistically significant differences between each configuration and the in vivo measurements.

	Subject K5R		*Subject K8L*	
Configuration	**Total TF force**		**Total TF force**	
	% Sig	**RMSE**	**% Sig**	**RMSE**
Marker-driven	16.80	1.601	6.36	2.812
FE	18.05	2.399	19.48	2.511
FE-AP	42.72	1.084	17.12	0.450
FE-SI	4.31	2.715	8.79	3.747
FE-AP-SI	3.95	1.178	3.63	1.283

Table 5. Statistical comparison of estimated total TF forces against in vivo measurements during squatting for subjects K5R and K8L under each prescription configuration. Reported metrics are the percentage of the squatting activity with statistically significant differences (% Sig) and the RMSE (in BW) computed over those significant regions.

	Subject K5R		*Subject K8L*	
Configuration	**Δ Impulse**		**Δ Impulse**	
	Median	**IQR**	**Median**	**IQR**
Marker-driven	3.199	0.846	4.335	1.138
FE	5.383	0.602	6.737	1.711
FE-AP	3.441	0.244	1.102	0.863
FE-SI	3.596	0.718	5.815	2.832
FE-AP-SI	1.663	0.418	0.377	1.595

Table 6. Differences in total TF force impulse (Δ Impulse) relative to in vivo measurements during squatting for subjects K5R and K8L under each prescription configuration, reported as the median and IQR across all simulated trials. Impulse is expressed in BW·s.

the in vivo measurements. These overestimates are also reflected in the higher RMSE values. Moreover, the differences between prescription configurations were more pronounced than in the walking trials.

The FE and FE-SI prescription configurations further exacerbated the overestimation obtained with the simulations using marker data alone, with RMSE values consistently exceeding 2.3 BW and reaching up to 3.747 BW for subject K8L in the FE-SI configuration. This behaviour is also reflected in the impulse analysis, where these configurations produced the largest deviations from in vivo

measurements, particularly for K8L (median Δ Impulse of 6.737 BW·s for FE, and 5.815 BW·s for FE-SI).

In contrast, the FE-AP and FE-AP-SI configurations markedly reduced the overestimation, with predicted force profiles generally closer to in vivo measurements throughout the activity. This improvement was particularly evident in the deep flexion region, where the deviation from the in vivo profile was visibly smaller than in the marker-driven, FE, and FE-SI configurations. Consistent with this, these configurations also yielded the smallest impulse differences relative to in vivo, with the FE-AP-SI configuration producing the lowest median Δ Impulse values for both subjects (1.663 BW·s for K5R and 0.377 BW·s for K8L), indicating a substantial reduction in loading prediction error. Additionally, the FE-AP-SI configuration showed the lowest percentage of statistically significant difference from the in vivo force measurements, with values below 4% for both subjects.

3.2.3. Medial and lateral TF force estimations

Figures 9 and 10 show the estimated medial and lateral TF forces during the squatting task for each prescription configuration for subjects K5R and K8L, respectively. Table 7 summarises the statistical comparison between the estimated and in vivo TF compartment forces across all configurations for both subjects.

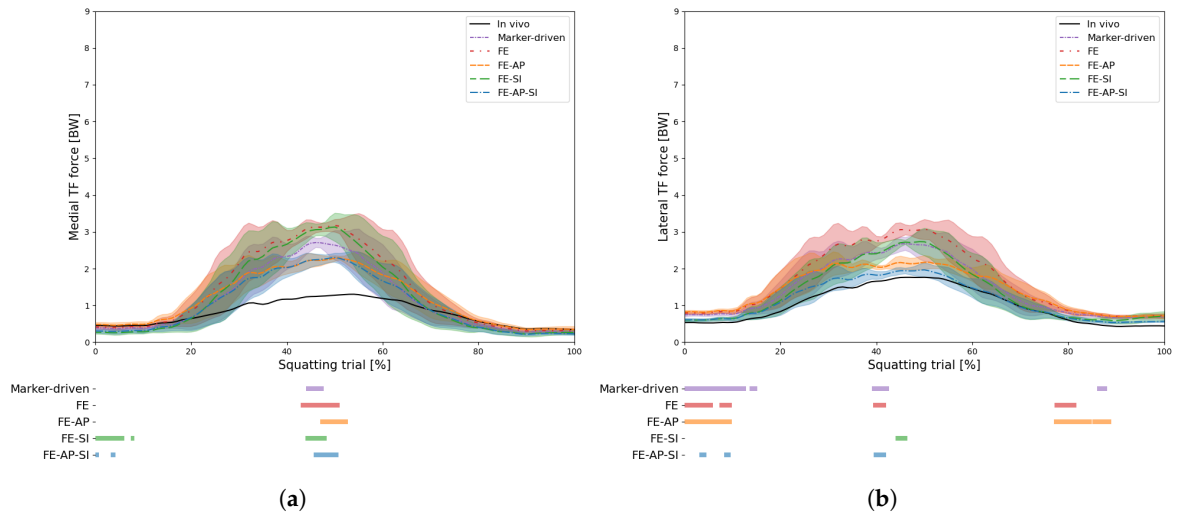

(**a**) (**b**)

Figure 9. Estimated medial (**a**) and lateral (**b**) TF force during squatting for subject K5R under each prescription configuration. The panels below each plot indicate regions of statistically significant differences between each configuration and the in vivo measurements.

During squatting, the medial and lateral TF force profiles showed consistent overestimation of load in both compartments across all prescription configurations for both subjects, with subject K8L exhibiting larger deviations from in vivo measurements. The discrepancies were generally greater in the medial compartment, while the lateral compartment loading remained relatively closer to the in vivo force profiles. This trend is also reflected in the RMSE values, which were generally higher for the medial than for the lateral compartment.

As observed for the total TF force, the FE and FE-SI configurations showed the largest overestimations of compartment loading, with medial TF force RMSE values reaching 1.870 BW and 1.776 BW for subjects K5R and K8L, respectively. Once again, the FE-AP and FE-AP-SI configurations reduced discrepancies in both compartments relative to the marker-driven simulations, yielding lower RMSE values and force profiles that were generally closer to in vivo measurements for both subjects. This improvement was particularly evident in the lateral compartment, where the estimated force profiles more closely matched the in vivo measurements in the deep flexion region, as evidenced by the lower RMSE values and reduced percentage of the squat with a significant difference relative to the in vivo measurements.

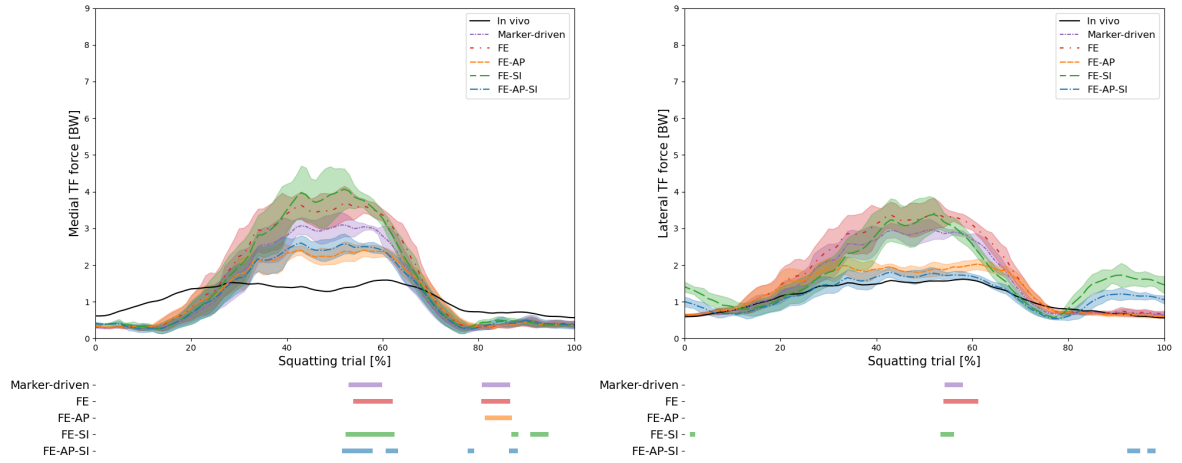

(**a**) (**b**)

Figure 10. Estimated medial (**a**) and lateral (**b**) TF force during squatting for subject K8L under each prescription configuration. The panels below each plot indicate regions of statistically significant differences between each configuration and the in vivo measurements.

Configuration	*Subject K5R*				*Subject K8L*			
	Medial TF force		**Lateral TF force**		**Medial TF force**		**Lateral TF force**	
	% Sig	**RMSE**	**% Sig**	**RMSE**	**% Sig**	**RMSE**	**% Sig**	**RMSE**
Marker-driven	3.58	1.451	20.01	0.407	12.86	1.149	3.72	1.297
FE	8.00	1.870	15.80	0.526	14.10	1.513	7.10	1.669
FE-AP	5.75	0.988	21.60	0.294	5.63	0.358	0.00	-
FE-SI	10.96	1.095	2.42	0.931	15.48	1.776	3.83	1.489
FE-AP-SI	6.90	0.860	5.31	0.136	12.05	0.908	4.31	0.560

Table 7. Statistical comparison of estimated medial and lateral TF forces against in vivo measurements during squatting for subjects K5R and K8L under each prescription configuration. Reported metrics are the percentage of the squatting activity with statistically significant differences (% Sig) and the RMSE (in BW) computed over those significant regions. Where no statistically significant differences were found, RMSE is not applicable (–).

3.2.4. Load distribution

The estimated MLR during the squatting trials is shown in Figure 11. The results indicate that the predicted MLR profiles were highly consistent across subjects and prescription configurations. In the deep flexion region, the predicted MLR was higher than the in vivo measurements for both subjects, consistent with the previously reported overestimations of the medial TF force. Moreover, the predicted MLR deviated from the in vivo curve at the beginning and end of the squat, with deviations more pronounced than those observed during walking. Deviations also appeared generally larger for subject K8L than for subject K5R, with both subjects exhibiting extensive regions of statistically significant differences from the in vivo curve.

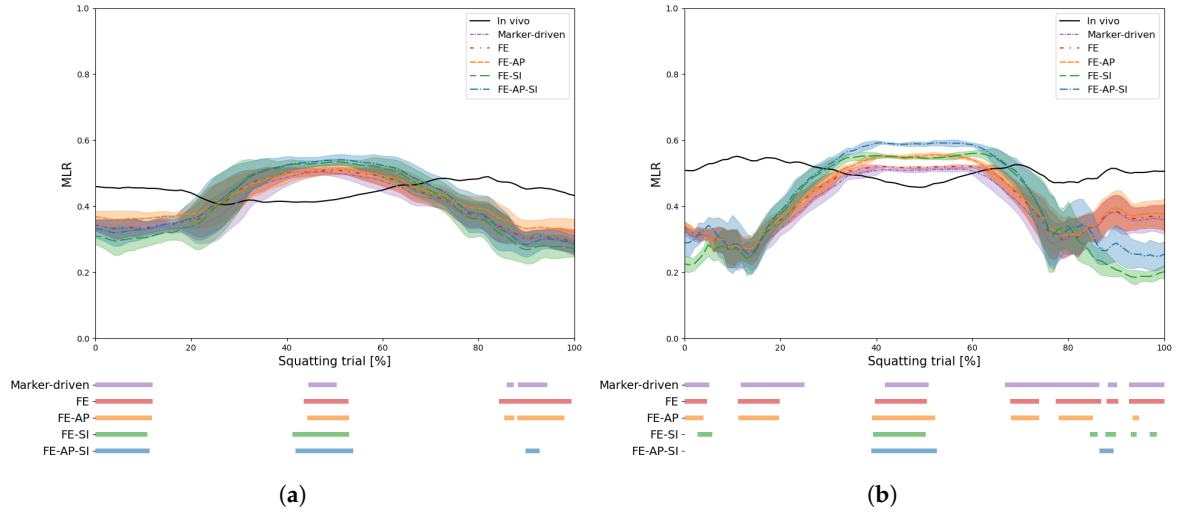

(**a**) (**b**)

Figure 11. Estimated MLR during squatting for subjects K5R (**a**) and K8L (**b**) under each prescription configuration.

3.2.5. Kinematic prescription strategy

Figure 12 presents a representative comparison between squat trial-specific and subject-level mean prescriptions for the FE-AP-SI configuration for subject K5R.

As observed in the walking simulations, the force curves for the trial-specific and subject-level mean prescriptions overlapped almost entirely, indicating that averaging the prescribed kinematic relationships at the subject level did not impact the estimated TF forces. Similar trends were observed for the FE-AP and FE-SI configurations. Comparable results for subject K8L are provided in Appendix F.

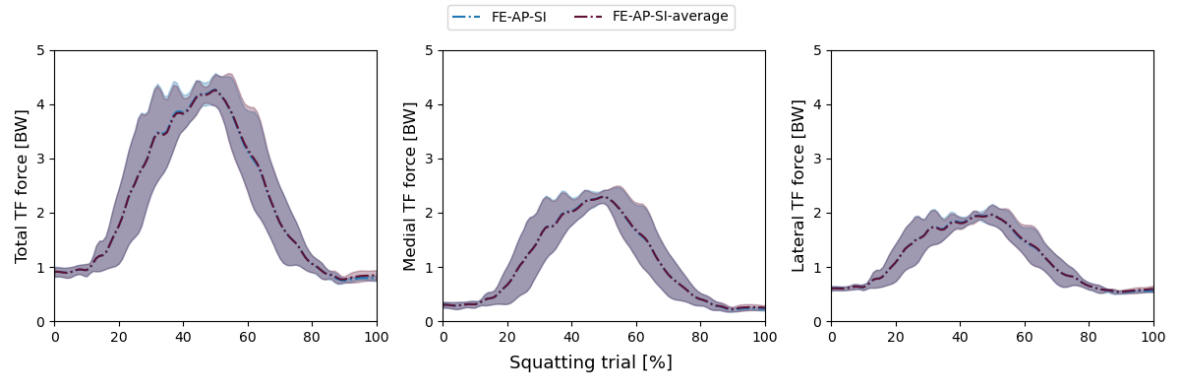

Figure 12. Comparison of cycle–specific and subject-level mean prescriptions for the FE-AP-SI configuration during squatting for subject K5R. Estimated total, medial, and lateral TF forces during squatting are shown for both approaches.

4. Discussion

This study aimed to develop and evaluate an MSK modelling framework that incorporates fluoroscopy-derived knee kinematics to estimate TF forces and medial-lateral load distribution. Specifically, this study examined, in two subjects and across two distinct activities, whether prescribing fluoroscopy-derived TF kinematics improved force estimates compared to simulations driven solely by marker data, and how distinct modelling choices affected the predicted knee loading and load distribution. The findings provide insight into how fluoroscopy-derived kinematics can be used as inputs to MSK models.

Walking and squatting were selected as complementary tasks because of their different kinematic and loading characteristics, with squatting involving larger flexion angles and higher joint loading.

This contrast enables the effects of prescribing fluoroscopy-derived kinematics to be evaluated under distinct movement conditions.

In general, the results demonstrate that fluoroscopy-derived kinematics substantially affect the predicted TF contact forces, with notable differences observed across prescription configurations in both activities. This can be explained by the fact that TF kinematics define the relative position and orientation of the femur with respect to the tibia and, consequently, the location and orientation of the joint rotation axis, which influences muscle moment arms. In particular, AP and SI translation, together with IE rotation, have been shown to be the DoFs that most strongly influence these moment arms [44,57]. These changes alter the muscle forces required to generate the joint moments, thereby affecting the muscle activations needed to reproduce the movement. Since muscle forces are the primary contributors to knee joint loading [58], these changes directly translate into differences in the estimated joint contact forces. In Appendix I, a schematic representation of how AP translation can change the muscle moment arm is presented.

4.1. Alterations in kinematics

As shown in the results section, although the overall shapes of the AP and SI translation curves remained similar to those of the original model parametrisations, the fluoroscopy-derived kinematics exhibited larger magnitudes and excursions. This likely reflects subject- and task-specific translational behaviour that generic parametrisations cannot fully capture. Such differences are biomechanically relevant, as alterations in AP and SI translations affect muscle moment arms and muscle force requirements, and are also expected to shift the TF contact locations throughout the movement. In turn, these changes may influence the distribution of load across the articular surface and the location of the CoP [58].

4.2. Walking simulations

The model driven solely by marker data produced TF force patterns during walking that were consistent with those reported in a previous MSK modelling study [52], indicating that the reference simulations align with established simulation approaches. Within this context, prescribing fluoroscopy-derived kinematics was assessed as a potential means of further improving these estimates.

Across both subjects, the marker-driven and FE configurations produced nearly identical force curves for all TF force components. This was expected, as the flexion profiles derived from marker-based motion capture were highly similar to those obtained from fluoroscopy. This is consistent with previous studies showing that knee flexion angles are generally well estimated using motion capture systems [59,60]. This suggests that prescribing fluoroscopy-derived FE alone does not lead to meaningful improvements in the predicted TF loading during walking.

Prescribing the two remaining in-plane DoFs produced more pronounced changes in model behaviour. In particular, AP translation increased the first and second peaks of the total TF compressive force in both subjects, suggesting that the predicted loads are sensitive to this translational DoF, as expected. A possible explanation for the increase in TF force is that, in both participants, AP prescription led to increased activation of the quadriceps muscles included in the analysis (rectus femoris, vastus lateralis and vastus medialis; see Appendix H). Despite this increase in peak magnitude, the FE-AP configuration yielded the best overall agreement with in vivo data for subject K5R, with no regions differing significantly during stance according to the statistical analysis.

In contrast to the FE-AP configuration, prescribing SI translation alongside FE led to markedly different model behaviour, with considerably larger discrepancies between predicted and in vivo TF forces. In both subjects, the FE-SI configuration introduced an additional increase in the total TF force during mid-stance, appearing almost as a third peak within the stance phase. This suggests that SI prescription substantially altered muscle moment arms and activation patterns. More specifically, it not only increased the activation of certain muscles, particularly the gastrocnemii, but also induced muscle activity during phases of stance in which this was not observed in other configurations, as seen for the semitendinosus (see Appendices G and H). In addition, the imposed SI kinematics may have

contributed directly to an increase in compressive TF loading by shifting the femur to a more inferior position relative to the tibia.

Although this behaviour was observed in both subjects, it was considerably more pronounced in K8L, likely because this subject exhibited a larger SI excursion, leading to greater changes in muscle moment arms. This larger SI excursion may be related to the larger femoral condyle size in K8L, as SI translation is linked to the condylar geometry of the knee joint. Notably, in subject K8L, these altered muscle activations were also accompanied by a marked shift in the medial-lateral load distribution. This can be explained by a change in the moment arm of the gastrocnemius medialis. As its moment arm decreased and even became negative during mid-stance, greater activation of the gastrocnemius lateralis was required to generate the same net knee joint moment. The resulting increase in gastrocnemius lateralis force contributed to the observed shift in load towards the lateral compartment.

A possible explanation for these findings is that AP and SI translations are mechanically coupled in the knee joint through the rolling and gliding behaviour of the femoral condyles [61]. As a result, prescribing SI translation alone, while maintaining the original model relationship for AP translation, may introduce a kinematic inconsistency in the sagittal plane. Although the model-defined AP and SI relationships follow trends similar to those observed in the fluoroscopy-derived data, their ranges differ, potentially leading to unrealistic combinations of joint translations when only one DoF is prescribed. This may partly explain the abnormal muscle mechanics observed in the FE-SI configuration and the more stable, physiologically plausible behaviour observed when AP and SI were prescribed simultaneously in the FE-AP-SI configuration.

Overall, the FE-AP-SI configuration yields better results than FE-SI, but appears to perform less well than FE-AP alone. This indicates that although prescribing both translational DoFs simultaneously may reduce the kinematic inconsistency associated with the FE-SI configuration, including SI translation still appears to negatively affect the estimation of TF forces during walking. Within this modelling framework, AP translation appears to provide useful subject-specific information during walking, whereas SI translation is more difficult to prescribe reliably.

Notably, for both subjects, the lateral TF force was more sensitive to the prescribed kinematics, as reflected by greater variation in lateral force curve shape across the prescription configurations. Regarding the medial-lateral load distribution, the MLR results (Figure 5) are consistent with the previous observations and further highlight that model performance was subject-dependent. Moreover, the deviations observed at the beginning and end of the gait cycle for the MLR should be interpreted with caution, as compressive TF forces in these regions remained below the 1000 N threshold for which the medial force estimation method is valid. These discrepancies may therefore partly reflect limitations of the estimation approach rather than model error.

4.3. Squatting simulations

As observed in the walking simulations, the marker-driven model also produced squat force estimates that agreed with those reported by Nejad et al. [52]. For the squatting simulations, the results were more consistent across subjects, with all prescription configurations leading to a marked overestimation of the TF forces.

In contrast to the walking simulations, prescribing FE further increased the overestimation relative to the marker-driven configurations. This may be explained by the higher flexion angles observed for this configuration, which are likely to increase joint loading. More generally, this observation suggests that marker-based motion capture may be less capable of accurately reproducing knee flexion during high-flexion tasks, such as squatting, than during walking, where the flexion range is smaller, and the differences between marker- and fluoroscopy-derived kinematics appear less pronounced.

Consistent with the walking trials, adding SI translation to the prescribed flexion angle did not improve force estimates and was generally associated with the largest increases in muscle activation. As discussed previously, this may be explained by the mechanical coupling between AP and SI translations in the knee joint. Prescribing SI translation independently of AP translation may therefore

increase joint compression and amplify the predicted contact forces, while failing to account for the coupled AP motion that normally accompanies SI translation, even more relevant during high-flexion activities.

On the other hand, configurations including AP translation appeared to improve the TF force estimates relative to the marker-driven simulations during squatting. In particular, the FE-AP-SI configuration substantially reduced the overestimations obtained with the marker-driven model, resulting in force curves that were much closer to the in vivo measurements and with small regions of statistically significant difference. This suggests that incorporating subject-specific AP translation provides a more realistic representation of TF joint kinematics, likely because AP motion plays a central role in shifting the contact location and the resulting muscle force requirements during flexion.

Despite the improvements achieved by prescribing the three in-plane DoFs from the fluoroscopy data, the model still consistently overestimated the TF forces across all prescription configurations. One possible explanation is that IE rotation is a relevant component of TF kinematics during squatting [62], yet it cannot be prescribed in the present simulations because it cannot be determined accurately with a monoplanar fluoroscopy system. Consequently, this rotational DoF remained driven by the model's generic kinematic relationships, which may have contributed to discrepancies in the predicted joint loading.

Additionally, the muscle activation patterns may help explain the persistent overestimation of the TF forces (see Appendix H). During squatting, some muscles reached activation levels of 1.0, particularly the biceps femoris long head and rectus femoris in both subjects, with the tibialis anterior also reaching saturation in K5R. This saturation suggests that the squatting task imposed mechanical demands that the model could not satisfy, given its available muscle force capacity and actuator setup. In particular, the optimal actuator force was not adjusted across simulations and may therefore have been insufficient for the higher joint moments associated with squatting. As a result, the muscles had to compensate, leading to activation saturation. This indicates that further improvements in the predicted TF forces may be achievable by tuning the actuator setup.

Regarding the estimated MLR, the simulations did not accurately reproduce the in vivo load distribution for either subject under any prescription configuration. In the deep flexion region, the predicted MLR was too high, consistent with the large overestimations of the medial TF force in this phase. At the beginning and end of the squat, the opposite trend was observed, with lower predicted MLR values due to relatively greater lateral and lower medial loading. As in walking, these discrepancies may partly be explained by limitations in the force estimation approach at low compressive TF force magnitudes. Overall, these findings suggest that improvements in total and compartmental TF force prediction did not translate into a more accurate representation of medial-lateral load distribution during squatting.

4.4. Overall interpretation of kinematic prescription effects

The comparison between walking and squatting simulations indicates that the effects of prescribing fluoroscopy-derived kinematics are task-dependent. For walking, the marker-driven simulations already provided a reasonable representation of TF loading, and the inclusion of fluoroscopy-derived kinematics resulted in limited changes, without consistent improvement in agreement with the in vivo measurements. This is consistent with previous studies, which have also reported limited improvements when incorporating subject-specific kinematics in gait simulations [45]. In contrast, for squatting, prescription configurations FE-AP and FE-AP-SI, particularly the latter, led to substantially improved agreement with the in vivo TF forces compared to the marker-driven model.

A possible explanation for this difference between tasks is that the MSK model used in this study has only been validated for walking and running. Its generic kinematic parametrisations are therefore likely more appropriate for walking than for a functionally distinct movement such as squatting, where they may be less representative of the underlying joint mechanics. As a result, incorporating more accurate subject-specific kinematics becomes more relevant in squatting.

In addition, model performance appeared to be subject-dependent, with overall more accurate predictions for subject K5R. For walking, these differences were already clearly visible in the marker-driven simulations, with the predicted TF forces for K5R remaining consistently closer to the in vivo measurements. In contrast, for subject K8L, the marker-driven configuration already overestimated the second stance peak, and prescribing fluoroscopy-derived kinematics did not lead to any clear improvement. This suggests that the inaccuracies in the predicted forces cannot be attributed solely to limitations in marker-based kinematics, but may also reflect modelling errors arising from assumptions inherent to the modelling framework. For squatting, the discrepancies between subjects were less pronounced, although the predictions for K8L still appeared to perform slightly worse than those for K5R.

Lastly, the comparison of prescription strategies showed that subject-specific averaged kinematics yielded results nearly identical to those obtained with cycle– and trial-specific prescriptions for walking and squatting, respectively, for both subjects. This was expected for subject K8L, given the high kinematic uniformity across trials, but was less anticipated for K5R, whose kinematics were much more heterogeneous. Nonetheless, these findings indicate that the modelling framework can be simplified by using subject-specific mean parametrisations without loss of accuracy. Additionally, they support the adequacy of spline interpolation for representing the prescribed kinematic relationships.

4.5. Limitations and future work

There are some limitations to consider when interpreting the results of this project. First, the MSK model used in this work assumes a native knee and the prescribed kinematics were derived from subjects with TKA. Therefore, part of the observed kinematic mismatch may also reflect differences between native and implanted knee joint mechanics, rather than task- and subject-specific kinematic variation alone. Moreover, previous studies have shown that TKA knees can exhibit greater kinematic excursions, particularly in the AP direction, with greater anterior tibial translation [63,64], consistent with the kinematic patterns observed in the present study.

Another limitation is that the simulations were conducted with only two subjects, limiting the generalisability of the findings. In addition, only two activities were investigated. Future work should extend the analysis to a larger number of subjects and a broader range of activities to further evaluate and get more robust conclusions on the effects of prescribing fluoroscopy-derived kinematics in MSK models. Moreover, the limited number of available trials per subject for both walking and squatting weakened the statistical analysis.

A further limitation concerns the reconstruction and implementation of the fluoroscopy-derived kinematics. Although subject-specific implantation data were used to guide the positioning of the implant geometries within the scaled MSK model, this procedure still relied partly on visual inspection and could have introduced small alignment errors. The absence of subject-specific skeletal geometries further complicated this implant positioning. Incorporating subject-specific bone geometries could improve the alignment between the implant frames and the model-defined joint reference frames, thereby enhancing the overall consistency of the reconstructed kinematics.

In addition, only the in-plane DoFs were prescribed from the fluoroscopy data, while the out-of-plane DoFs remained driven by the model's generic kinematic parametrisations. As discussed before, this may have introduced inconsistencies in the overall joint kinematics and affected the predicted loading patterns. Moreover, these out-of-plane DoFs are highly relevant for joint loading estimations. Further research should investigate integrating out-of-plane DoFs as kinematic inputs to the MSK model, provided that biplanar fluoroscopy data are available.

Furthermore, modifying the parametrisations of the AP and SI translations directly in the model file enforces these kinematics rigidly throughout the simulation. Consequently, these DoFs cannot adapt to the interactions with the remaining model coordinates during the IK step. This may introduce further errors and prevent the model from achieving a fully mechanically consistent solution, potentially affecting the predicted joint loading.

In addition, the available EMG data could be further exploited within the modelling framework. Incorporating these data into EMG-informed MSK models would enable a more subject-specific representation of muscle recruitment, including the effects of muscle co-contraction, and may improve the accuracy of the predicted joint loading.

Lastly, future work could explore the use of more advanced modelling frameworks. For instance, the Joint Articular Mechanics (JAM) MSK model provides a more detailed representation of the knee joint, including multiple DoFs and ligament structures [65]. Such a framework would eliminate the need for predefined kinematic parametrisations, and incorporating fluoroscopy kinematics would be more straightforward, as these could be prescribed directly during the IK step rather than imposed through modifications to the model file. This could reduce the kinematic inconsistencies described previously, since the non-prescribed DoFs would be free to settle into equilibrium during the optimisation. In addition, the model enables the estimation of load distributions within the TF joint. Building on this, further developments could aim to derive CoPs from these load distributions, thereby providing additional insight into joint contact mechanics.

5. Conclusions

This study successfully developed and implemented a modelling framework to integrate fluoroscopy-derived knee kinematics into a generic MSK model, enabling evaluation of how prescribing fluoroscopy-derived TF kinematics affects predicted joint loading. For walking, incorporating fluoroscopy-derived kinematics did not result in consistent or significant improvements in the estimated TF loads, compared with simulations driven solely by marker data. In contrast, for squatting, the FE-AP and FE-AP-SI prescription configurations consistently improved TF force predictions compared with marker-driven simulations.

The results further showed that the chosen prescription configuration clearly influenced the estimated knee loading, whereas comparing prescription strategies indicated that subject-level averaging of kinematic relationships did not meaningfully affect the predicted forces. Therefore, the modelling framework can be simplified without compromising prediction accuracy. Despite improvements, the medial-lateral load distribution remained difficult to estimate accurately during squatting.

Overall, the improvements in TF force predictions observed during squatting highlight the potential of incorporating fluoroscopy-derived kinematics into generic MSK models, particularly for tasks that may not be well represented by generic modelling assumptions. Future work should therefore focus on evaluating the proposed framework across a broader range of dynamic tasks and subjects, and on integrating all six DoFs of fluoroscopy-derived kinematics to further improve model performance.

By improving the estimation of TF joint loading, integrating fluoroscopy-derived kinematics has the potential to overcome the limitations of current MSK models and measurement approaches, contributing to a more accurate and comprehensive understanding of knee joint biomechanics. Ultimately, this may provide deeper insight into the biomechanical pathways underlying knee OA and enable more informed approaches to its analysis, prevention, and treatment.

List of abbreviations

AP	Anterior-posterior
BW	Body Weight
CAMS	Comprehensive Assessment of the Musculoskeletal System
CoPs	Centre(s) of Pressure
CS	Coordinate System
DoF(s)	Degree(s) of Freedom
EMG	Electromyography
FE	Flexion-extension
GRF(s)	Ground Reaction Force(s)
ID	Inverse Dynamics
IE	Internal-external
IK	Inverse Kinematics
ML	Medio-lateral
MLR	Medial Load Ratio
MSK	Musculoskeletal
OA	Osteoarthritis
PF	Patellofemoral
RMR	Rapid Muscle Redundancy
RMSE	Root-mean-squared Error
SI	Superior-inferior
SPM	Statistical Parametric Mapping
TF	Tibiofemoral
TKA	Total Knee Arthroplasty
VV	Varus-valgus

Appendix A. Coordinate Systems and Transformations in the CAMS-knee Dataset

In the CAMS-knee dataset, four main coordinate systems are defined:

- CS_{LAB}: coordinate system of the motion capture laboratory; all motion capture and force plate measurements are reported in this coordinate system.
- CS_{JWI}: local coordinate systems fixed to the implant components; the in vivo TF contact forces and moments measured by the instrumented implant are expressed in $CS_{JWI_{tib}}$.
- CS_{LMB}: local coordinate systems fixed to the tibia and femur bones; the fluoroscopic measurements of implant kinematics are reported as a transformation from this coordinate system to CS_{LAB}.
- CS_{CT}: coordinate system of the computed tomography (CT) images; the position of anatomical landmarks is presented in this coordinate system, and the subject-specific implantation data are reported as transformations from CS_{JWI} coordinate systems to CS_{CT}

Data can be transformed between all four CS definitions by using the transformation matrices $\boldsymbol{T}_{JWI\rightarrow LMB}$, $\boldsymbol{T}_{JWI\rightarrow CT}$, and $\boldsymbol{T}_{LMB\rightarrow LAB}$. The first two are static and for each subject, and are provided in the dataset description. The transformation matrix $\boldsymbol{T}_{LMB\rightarrow LAB}$ is reported for each time step in the main data file of the dataset.

Appendix B. Transformation of fluoroscopy-derived kinematics to MSK model joint frames

In this section, $\boldsymbol{T}_{A\rightarrow B}$ denotes the transformation matrix that expresses coordinates from frame A in frame B.

In the dataset, the fluoroscopic implant kinematics are provided as the transformations of the tibial and femoral LMB implant frames with respect to the global laboratory frame CS_{LAB}, i.e., as $\boldsymbol{T}_{tib_{LMB}\rightarrow LAB}$ and $\boldsymbol{T}_{fem_{LMB}\rightarrow LAB}$. From these, the relative TF transformation was first reconstructed between the tibial

and femoral LMB frames and subsequently expressed in CS_{JWI}, yielding $\boldsymbol{T}_{tib_{JWI} \rightarrow fem_{JWI}}$. This was done as follows:

$$\boldsymbol{T}_{tib_{LMB} \rightarrow fem_{LMB}} = \boldsymbol{T}_{LAB \rightarrow fem_{LMB}} \cdot \boldsymbol{T}_{tib_{LMB} \rightarrow LAB} \tag{A1}$$

$$\boldsymbol{T}_{tib_{JWI} \rightarrow fem_{LMB}} = \boldsymbol{T}_{tib_{LMB} \rightarrow fem_{LMB}} \cdot \boldsymbol{T}_{tib_{JWI} \rightarrow tib_{LMB}} \tag{A2}$$

$$\boldsymbol{T}_{tib_{JWI} \rightarrow fem_{JWI}} = \boldsymbol{T}_{fem_{LMB} \rightarrow fem_{JWI}} \cdot \boldsymbol{T}_{tib_{JWI} \rightarrow fem_{LMB}} \tag{A3}$$

An additional transformation step was required to express the fluoroscopy-derived kinematics in the reference frames defining the knee joint in the MSK model. For this purpose, the implant geometries, whose local reference frames are defined in CS_{JWI}, were positioned on the scaled model in OpenSim Creator. The femoral component was first aligned by visual inspection. Subsequently, the tibial component was positioned relative to the femoral component using the subject-specific implantation data, specifically the translational parameters. Figure A1 illustrates the positioning of the implant geometries in one of the scaled models.

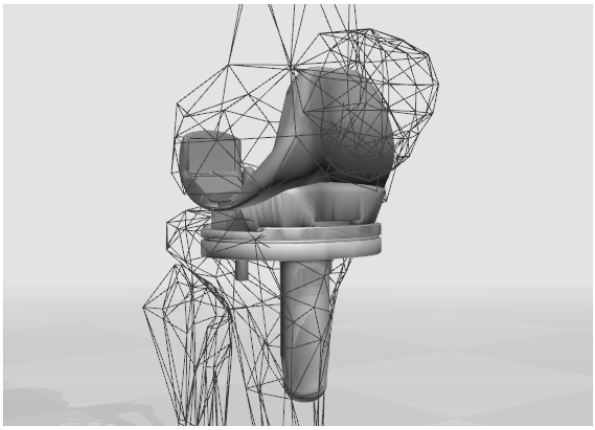

Figure A1. Positioning of the implant CAD geometries on the scaled femur and tibia for subject K5R, illustrating the alignment of the implant components with the bone geometries.

The implant positioning was performed solely to determine the transformations between the JWI coordinate systems and the reference frames defining the knee joint in the MSK model, namely $\boldsymbol{T}_{tib_{JWI} \rightarrow tib_{offset}}$ and $\boldsymbol{T}_{fem_{JWI} \rightarrow fem_{offset}}$. This was done using OpenSim Creator, after which the implant geometries were removed and were not included in the final simulation models. The final transformation between the tibial and femoral reference frames was obtained as:

$$T_{tib_{offset} \rightarrow fem_{offset}} = T_{fem_{JWI} \rightarrow fem_{offset}} \cdot T_{tib_{JWI} \rightarrow fem_{JWI}} \cdot T_{tib_{offset} \rightarrow tib_{JWI}} \tag{A4}$$

The transformation was formulated from the tibia to the femur because, in the MSK model, the tibia defines the child frame and the femur the parent frame of the knee joint. The TF translations and rotations were extracted from the final transformation matrices.

Appendix C. Parametrisations of TF AP and SI translations as functions of knee flexion

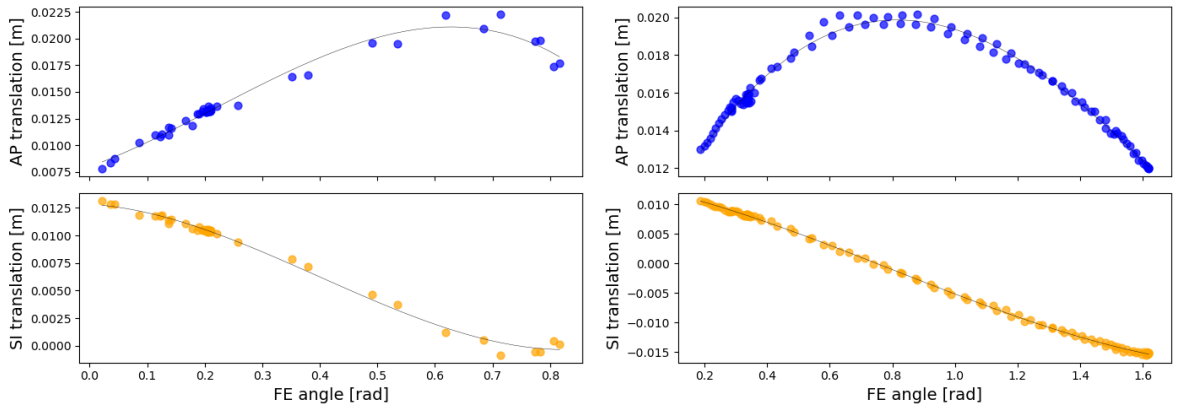

(**a**) (**b**)

Figure A2. Example of polynomial fitting of AP (top) and SI (bottom) translations as functions of knee flexion for subject K5R, shown for a gait cycle (**a**) and a squatting cycle (**b**). Scatter points represent the original fluoroscopy data, and the solid lines represent the fitted curves.

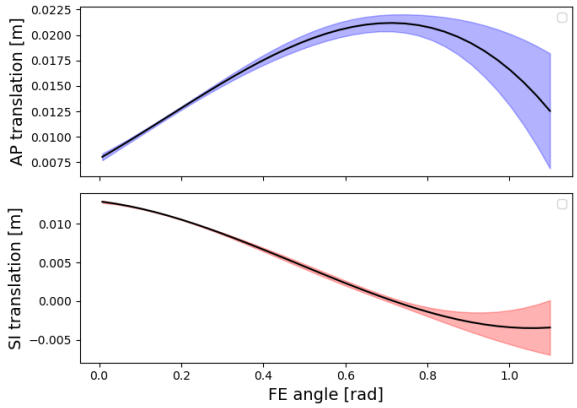

Figure A3. Subject specific mean AP (top) and SI (bottom) translation-flexion relationships during walking for subject K5R, obtained by averaging the fitted curves across cycles. Shaded regions indicate the standard deviation.

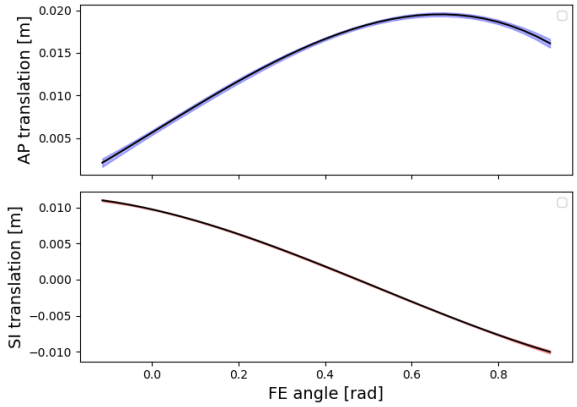

Figure A4. Subject specific mean AP (top) and SI (bottom) translation-flexion relationships during walking for subject K8L, obtained by averaging the fitted curves across cycles. Shaded regions indicate the standard deviation.

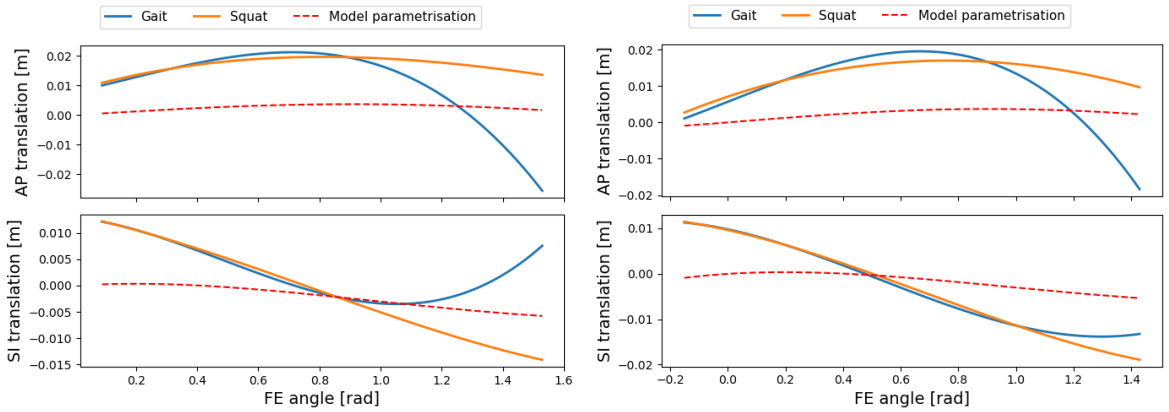

Figure A5. Comparison of spline-based TF kinematics derived from fluoroscopy data with the original model parametrisations for K5R (**a**) and K8L (**b**). The parametrisations were evaluated over the subject-specific maximum flexion range observed in the fluoroscopy trials.

Appendix D. RMR solver - cost function

For each time step t_k, the optimiser finds the optimal combination of muscle activations (a_k) and controls (c_k), by minimising the following cost function:

$$J(a_k, c_k) = \sum_{i=1}^{N_m} w_i a_{i,k}^2 + \sum_{j=1}^{N_q} v_j c_{j,k}^2 \tag{A5}$$

in which $a_{i,k}$ is the activation of muscle i at time step t_k, and $c_{j,k}$ corresponds to the control input of the actuator j at the same time step. The coefficients w_i and v_j are the weights that define the penalty on muscle activation and actuator use. The actuator set $c_{j,k}$ includes the actuators driving the trunk and the pelvis, as well as reserve actuators. In the presented cost function, the reserve actuators are assigned larger weights v_j than the muscle weights w_i, such that the solution remains predominantly muscle-driven and reserves are used only when necessary. In addition, the RMR formulation requires that each unlocked coordinate in the model be actuated, meaning there has to be at least one actuator per DoF.

Appendix E. Knee kinematics

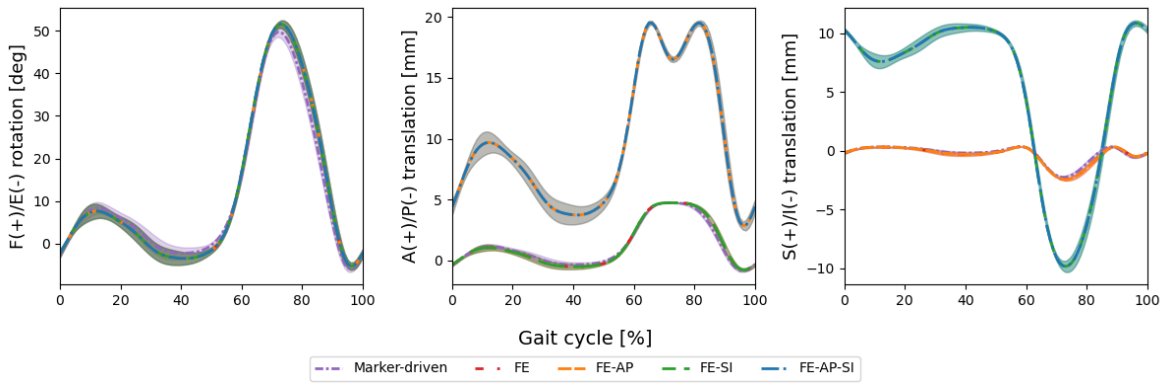

Figure A6. In-plane TF kinematics across the gait cycle for subject K8L under each prescription configuration, shown as mean ± 1 SD over six simulated gait cycles (n = 6).

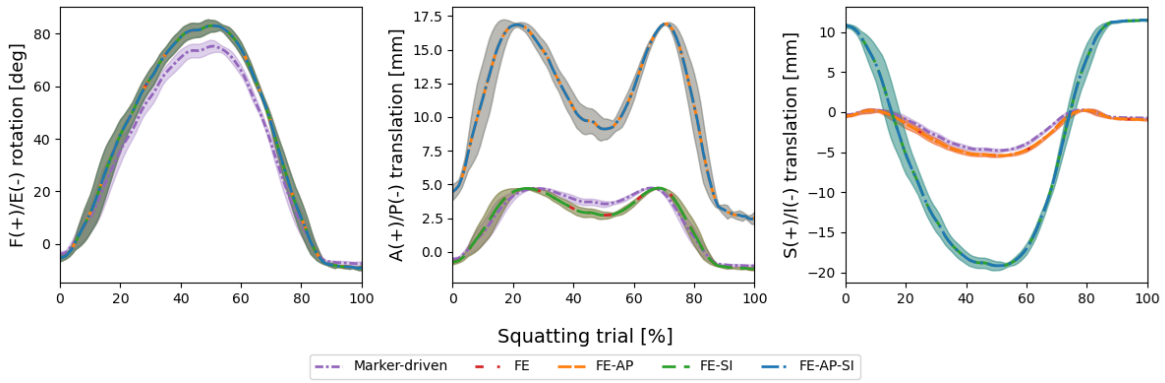

Figure A7. In-plane TF kinematics across the squatting trial for subject K8L under each prescription configuration, shown as mean ± 1 SD over five simulated squats (n = 5).

Appendix F. Kinematic prescription strategy - additional graphs

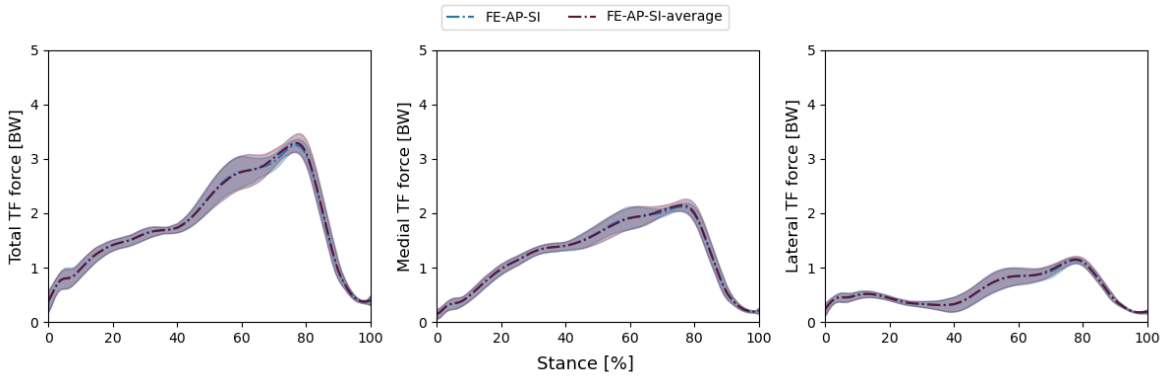

Figure A8. Comparison of gait cycle-specific and subject-level mean prescriptions for the FE-AP-SI configuration during walking in subject K8L. Estimated total, medial, and lateral TF forces across the stance phase of gait are shown for both approaches as mean ± 1 SD over six simulated gait cycles (n = 6).

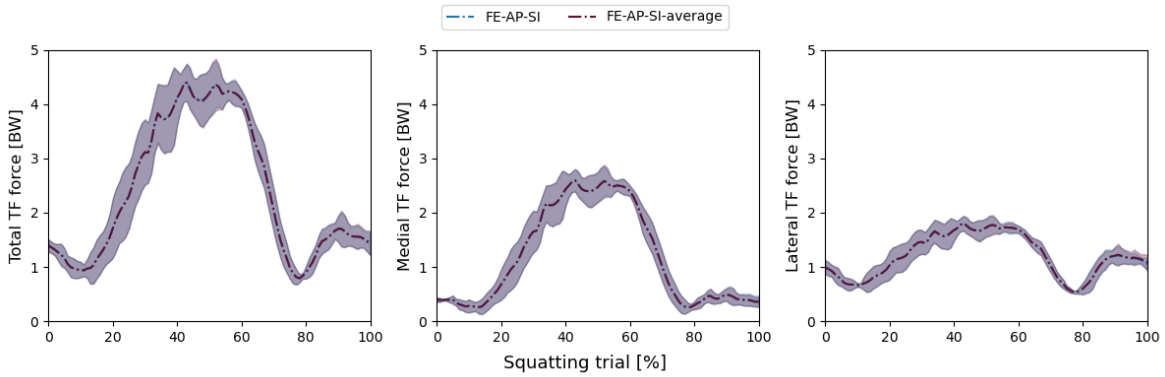

Figure A9. Comparison of cycle-specific and subject-level mean prescriptions for the FE-AP-SI configuration during squatting in subject K8L. Estimated total, medial, and lateral TF forces during squatting are shown for both approaches as mean ± 1 SD over five simulated squats (n = 5).

Appendix G. Muscle moment arms

Appendix G.1. Walking simulations

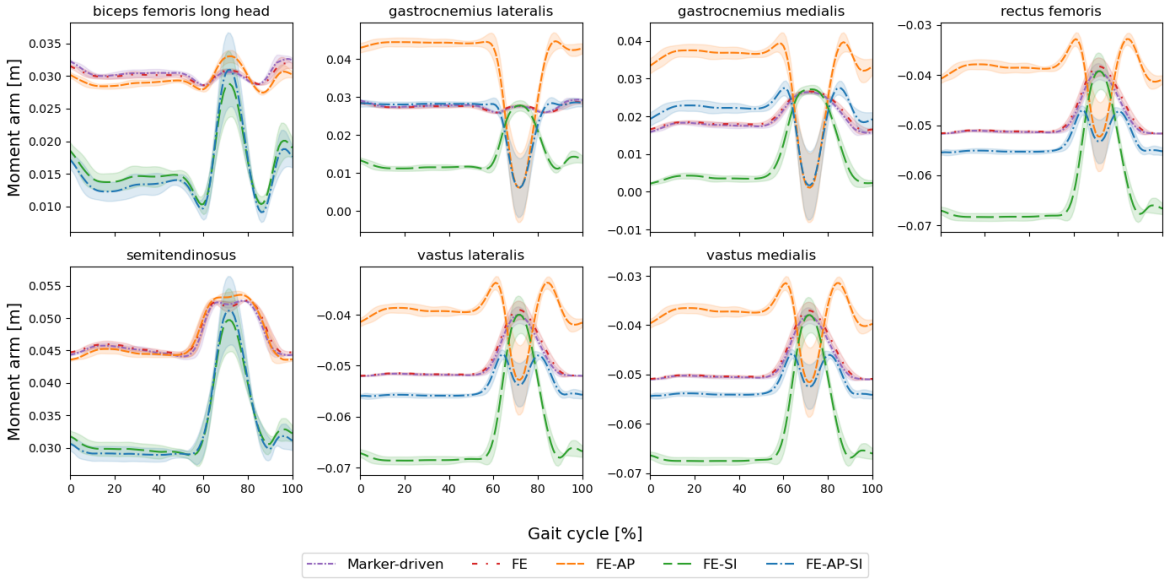

Figure A10. Estimated muscle moment arms about the knee joint across the gait cycle for subject K5R under each prescription configuration. Curves are shown as mean ± 1 SD over six simulated gait cycles (n = 6).

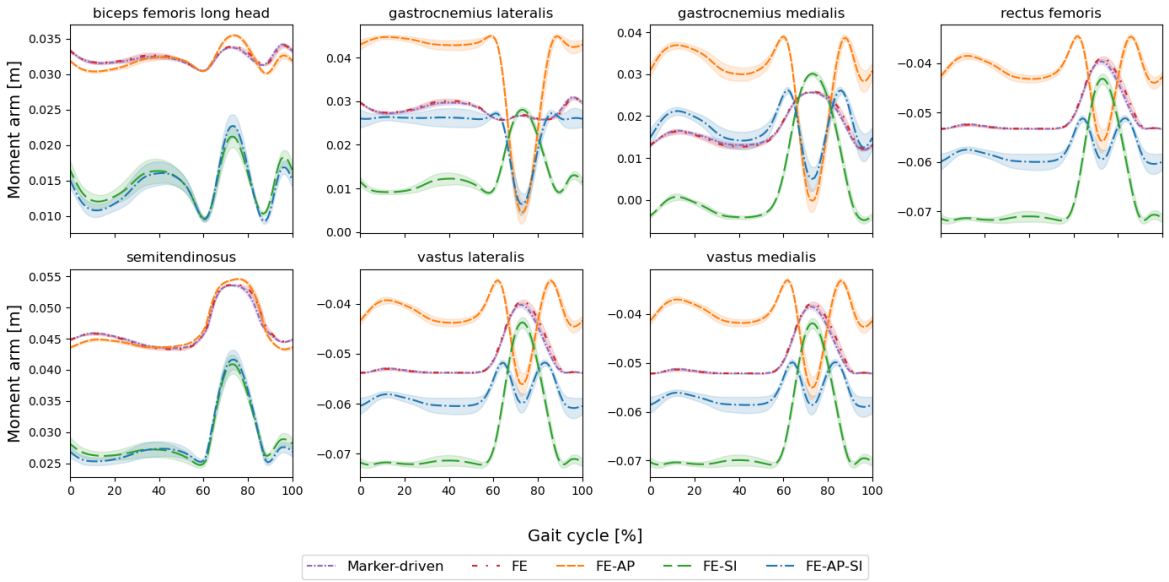

Figure A11. Estimated muscle moment arms about the knee joint across the gait cycle for subject K8L under each prescription configuration. Curves are shown as mean ± 1 SD over six simulated gait cycles (n = 6).

Appendix G.2. Squatting simulations

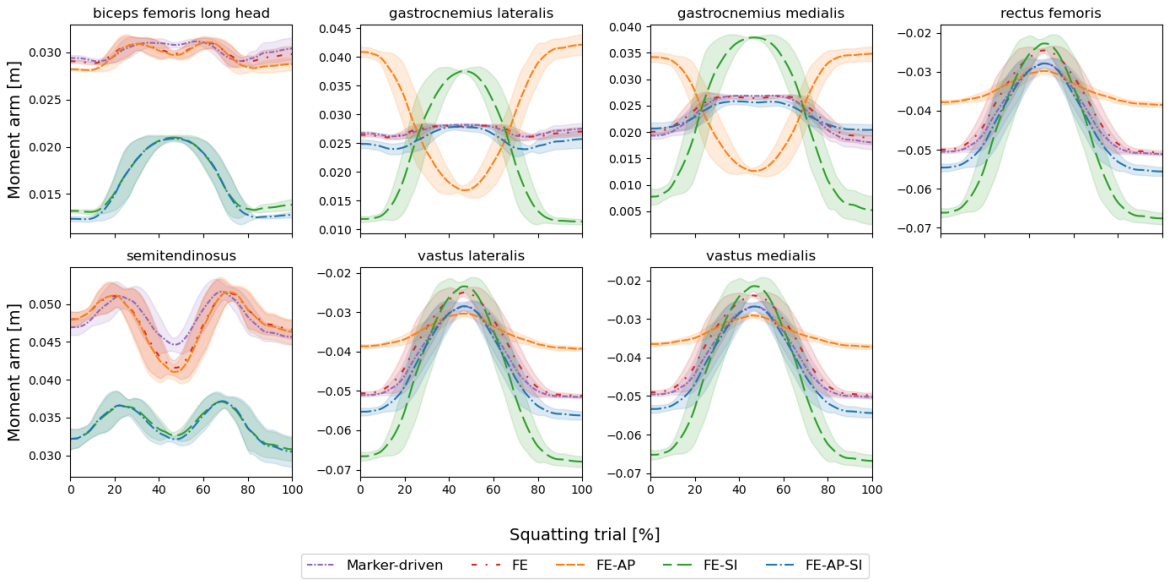

Figure A12. Estimated muscle moment arms about the knee joint during squatting for subject K5R under each prescription configuration. Curves are shown as mean ± 1 SD over five simulated squats (n = 5).

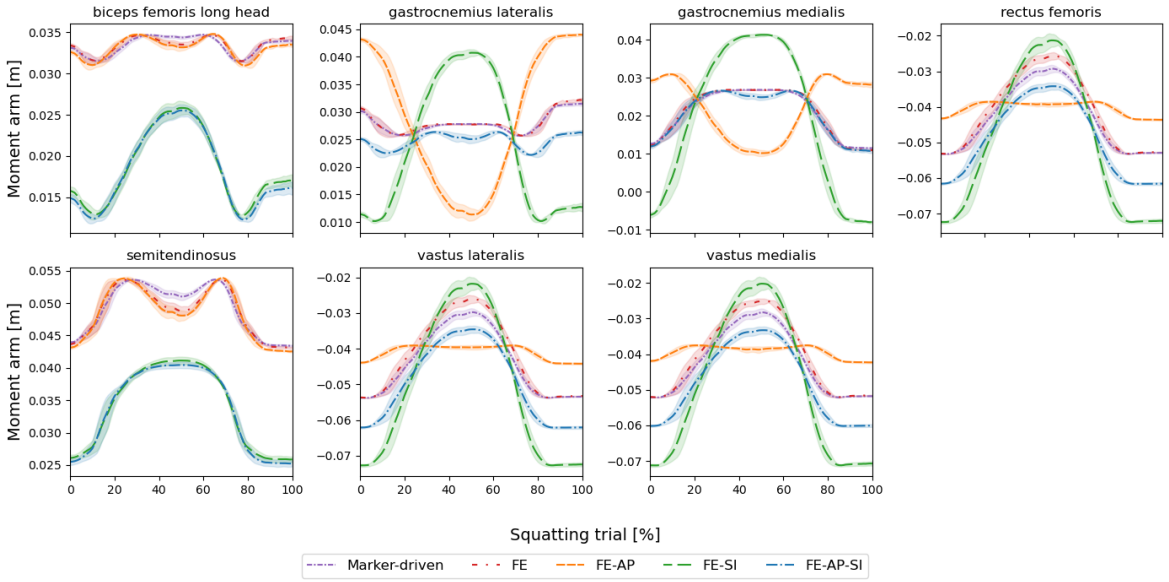

Figure A13. Estimated muscle moment arms about the knee joint during squatting for subject K8L under each prescription configuration. Curves are shown as mean ± 1 SD over five simulated squats (n = 5).

Appendix H. Muscle activations

Appendix H.1. Walking simulations

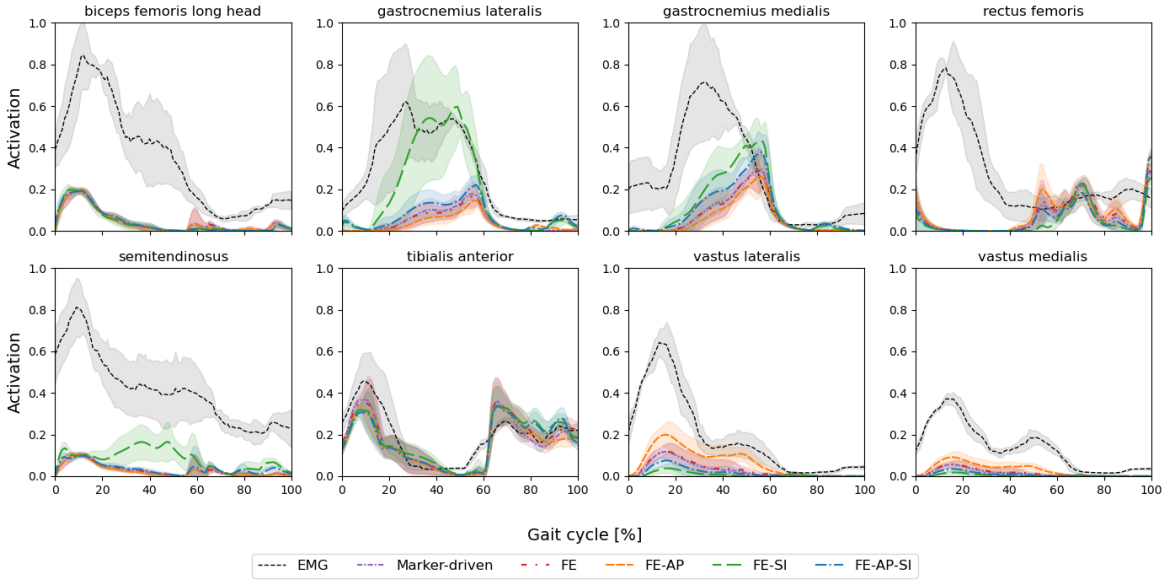

Figure A14. Estimated muscle activations across the gait cycle for subject K5R under each prescription configuration. Curves are shown as mean ± 1 SD over six simulated gait cycles (n = 6).

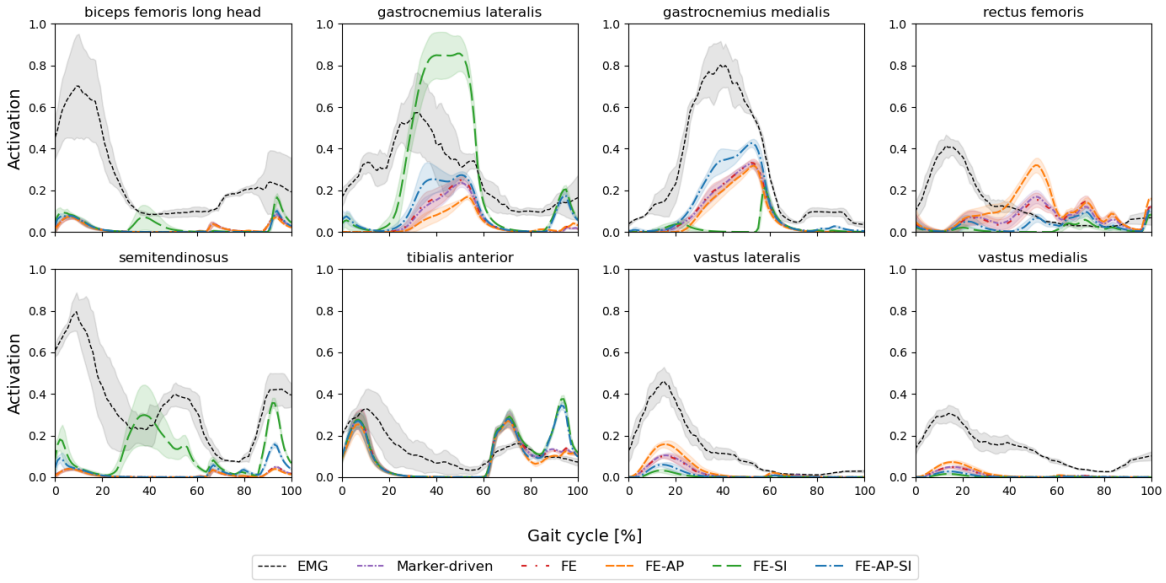

Figure A15. Estimated muscle activations across the gait cycle for subject K8L under each prescription configuration. Curves are shown as mean ± 1 SD over six simulated gait cycles (n = 6).

Appendix H.2. Squatting simulations

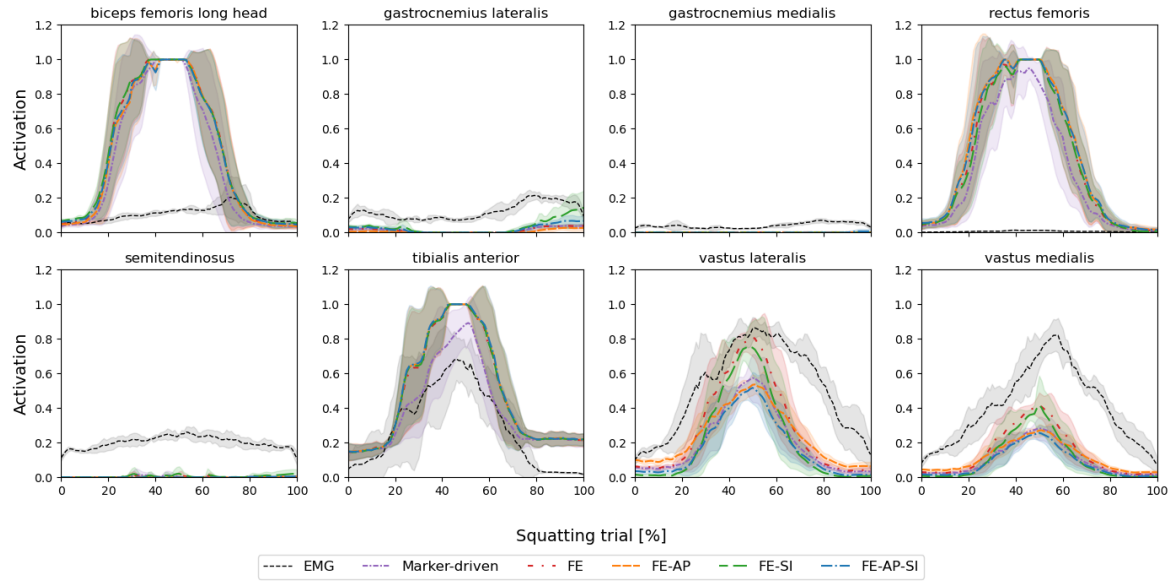

Figure A16. Estimated muscle activations during squatting for subject K5R under each prescription configuration. Curves are shown as mean ± 1 SD over five simulated squats (n = 5).

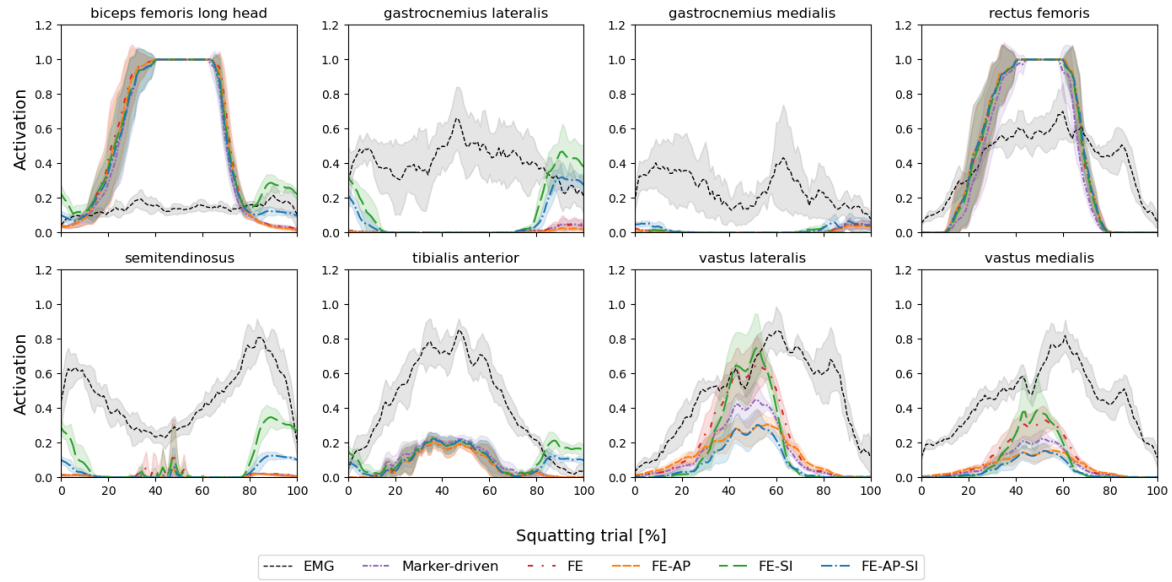

Figure A17. Estimated muscle activations during squatting for subject K8L under each prescription configuration. Curves are shown as mean ± 1 SD over five simulated squats (n = 5).

Appendix I. Illustration of the Effect of TF AP Translation on Muscle Moment Arm

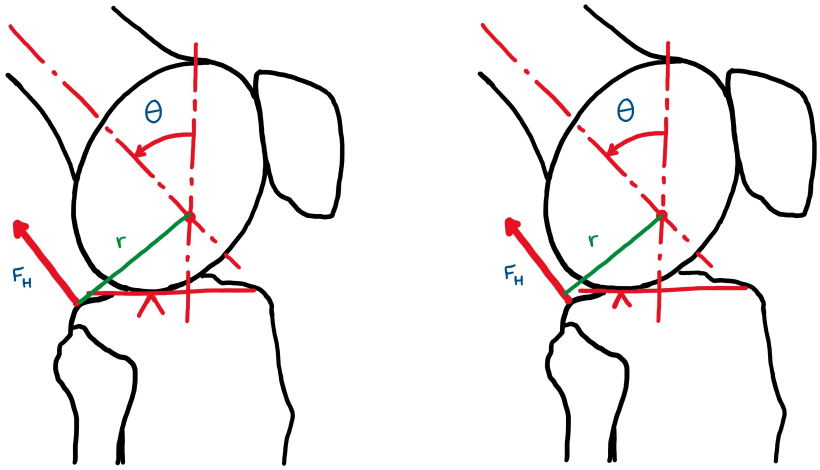

Figure A18. Schematic representation of the hamstring force F_H and its knee flexion moment arm r, illustrating the effect of altered TF AP translation on moment arm length. In the configuration on the right, the femur is translated posteriorly relative to the tibia, resulting in a decreased moment arm. The drawing is adapted from a figure from Delp et al. [66].

Appendix J. Initial Modelling Framework: JAM Model

This appendix documents the work developed during the early stages of this thesis, focusing on the implementation and evaluation of the JAM MSK model as the initial computational modelling framework. The reasons for its exclusion from the final methodology are also discussed.

Appendix J.1. Overview of the JAM model

The JAM model is a full-body MSK model featuring a detailed representation of the knee joint [65] (Fig. A19 (a)). The model comprises 52 DoFs and includes 44 Hill-type musculotendon units representing the musculature of the right lower limb. Given the characteristics of the dataset used in this study, which included participants with TKA, a TKA-specific version of the model was employed [67]. In this configuration, the knee joint is represented by a three-body TKA system, consisting of tibial, femoral, and patellar implant components that are appropriately positioned relative to the underlying bone geometries. Both the TF and PF joints are modelled with 6 DoFs and incorporate deformable contact between the articulating surfaces, based on an elastic foundation formulation, in which contact pressures are defined as functions of surface penetration depth.

Additionally, the model includes an extensive representation of ligaments and tendons within the knee joint. Specifically, it incorporates the patellar tendon and eleven ligament bundles. These model components are represented as non-linear spring elements. The anterior cruciate ligament was excluded from the model because it was resected during the TKA surgery of the patient used as the basis for model development [67]. While these detailed ligamentous representations enable a more physiologically realistic description of knee joint mechanics, they also increase the complexity of the model and can introduce additional sources of error.

Appendix J.2. Solution strategy - COMAK optimisation algorithm

For walking simulations, the JAM model is solved using the Concurrent Optimisation of Muscle Activations and Kinematics (COMAK) algorithm [68,69]. Within the COMAK framework (Fig. A19 (b)), model coordinates are grouped according to their role in the solution strategy. The primary coordinates include knee flexion of the leg of interest, hip rotations, and ankle flexion, which are obtained from marker-based motion capture data and used to drive the model dynamics. COMAK subsequently solves for the muscle and joint forces required to produce the corresponding accelerations.

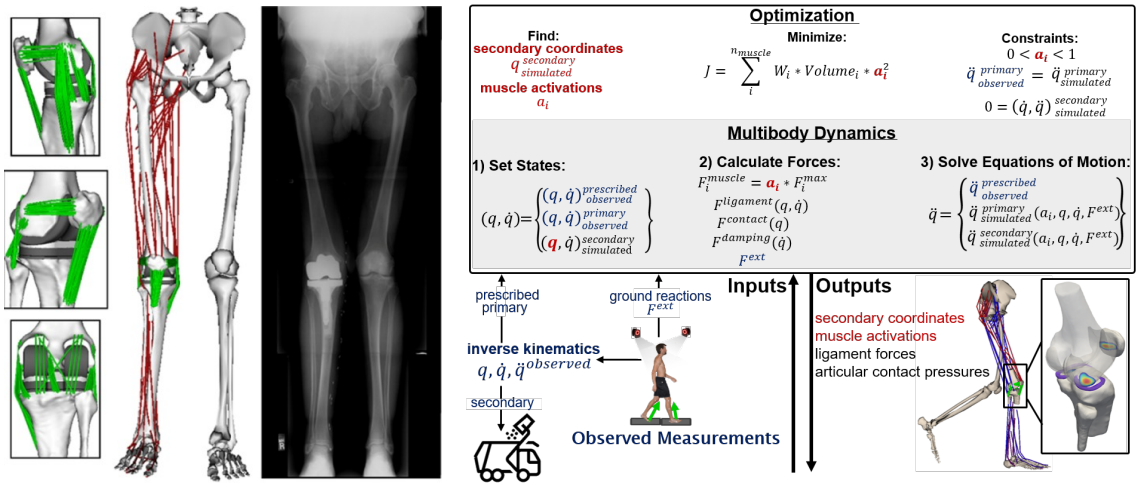

(**a**) (**b**)

Figure A19. (**a**) Illustration of the JAM MSK model of the right lower limb with TKA, showing the detailed knee joint representation and associated ligamentous structures, alongside a standing radiographic image used to define component alignment. (**b**) Schematic overview of the COMAK algorithm. The framework combines multibody dynamics with optimisation to estimate joint mechanics. Given prescribed inputs (primary IK-derived coordinates and GRFs), the model enforces the equations of motion while minimising a cost function. The resulting solution provides estimates of secondary kinematics, muscle activations, ligament forces, and articular contact pressures.

The secondary coordinates comprise all TF translations and non-sagittal rotations, as well as PF coordinates. These DoFs cannot be accurately measured using conventional motion capture techniques and are estimated by COMAK through optimisation. Solving these coordinates within the optimisation process also helps maintain dynamic consistency. The remaining coordinates, including those of the upper body, contralateral limb, and pelvis, are prescribed to the model as inputs and are not solved dynamically.

This algorithm begins with an IK step to determine the values, velocities, and accelerations of the primary coordinates from the measured marker data. During this step, the secondary coordinates are coupled to the independent coordinate, the knee flexion, through coordinate constraint functions. These constraint functions are generated via a passive forward simulation and incorporated into the IK formulation, yielding an IK solution that enforces the prescribed coupling between the primary and secondary coordinates.

Subsequently, the numerical optimisation takes place to estimate the secondary kinematics, as well as muscle, ligament and articular contact forces, by minimising the following cost function:

$$\min \sum_{i=1}^{n_{\text{Muscles}}} W_i * V_i * a_i^2 + CW \sum_{j=1}^{n_{\text{ContactForce}}} CE_j^2 \tag{A6}$$

where W_i, V_i and a_i represent the i-th muscle weight, volume, and activation, respectively, CW denotes the contact energy weight and CE the articular contact energy. This formulation enforces a balance between minimising muscle activation effort and net knee contact energy. The inclusion of the contact energy term is not always employed across studies, in which case the optimisation is driven solely by the muscle activation term.

Appendix J.3. Rationale for model selection

As previously mentioned, the JAM model was initially considered for this project for multiple reasons. First, it includes a highly detailed representation of the knee joint. Many widely used MSK models define the knee using simplified joint formulations, often with a single DoF and without explicit representation of ligamentous structures [37,47]. In such models, the remaining TF and PF DoFs are

commonly parametrised as functions of the knee flexion angle. While computationally efficient, these formulations do not enable estimation of ligament or cartilage loading profiles, structures that contribute to the stabilisation of secondary joint motion. Additionally, joint constraints are usually derived from cadaveric studies, failing to capture the load-dependent variations of joint kinematics [65].

In contrast, the JAM model defines both the TF and the PF joints with six DoFs and incorporates explicit ligament constraints, constructed based on imaging-derived anatomical data. This level of detail was considered advantageous for capturing joint behaviour beyond simplified kinematic assumptions.

Furthermore, the model incorporates deformable contact at the TF and PF joints using the elastic foundation formulation, as previously mentioned, thereby accounting for the elastic material properties of the articulating surfaces. This allows the COMAK algorithm to compute joint contact forces and surface pressure distributions. The ability to resolve contact pressure distributions was considered valuable, as it was hypothesised that changes in joint kinematics, resulting from the direct prescription of fluoroscopy-derived kinematics, could alter the spatial distribution of articular contact, based on the findings of previous studies [70].

An additional motivation for selecting the JAM model, especially its TKA-specific version, is that it facilitates subject-specific representation of implant geometry. In particular, the model implant components can be readily replaced and positioned using subject-specific implant geometries and implantation data provided in the dataset. Moreover, the framework allows straightforward prescription of in-plane TF kinematics derived from fluoroscopy within the IK step.

Together, these features made the JAM modelling framework a promising option to investigate how fluoroscopy-derived knee joint kinematics could be integrated into computational models to improve the estimation of joint mechanics.

Appendix J.4. Model adaptations

The JAM model was modified to incorporate the specific implant components from the CAMS-knee dataset, utilising the provided geometry files and aligning them according to subject-specific implantation data. Although the TKA configurations in the CAMS-knee dataset subjects did not include a patellar component, this element was retained in the model. This choice was motivated by the aim to limit additional modelling complexity associated with replacing the implanted patellar component with a native patella representation, which would require further modifications to ligament and muscle attachment sites and their associated properties. In addition, the presence of a patellar implant was expected to have a low influence on TF kinematics, provided that it did not impose additional constraints on joint motion.

For the contact surface geometries of the tibial and femoral implant components, computer-aided design software was used to extract the relevant mesh regions from the provided geometry files. Subsequently, the extracted surfaces underwent a cleaning procedure and were remeshed to obtain suitable contact meshes. The resulting triangulated surfaces were defined to match the element count of the original implant designs.

The final model was then scaled on the OpenSim GUI to match the subject's anthropometry. All subsequent steps of the COMAK analysis workflow were executed via the OpenSim command-line interface using customised settings files.

Appendix J.5. Simulations

A series of walking simulations was performed using the adapted JAM model to evaluate its behaviour under different kinematic and solver configurations. Initial simulations focused on single gait cycle analyses without prescription of fluoroscopy-derived kinematics. These simulations were repeated multiple times, for distinct gait cycles, adjusting some optimisation parameters and model

components. At a later stage, simulations with prescribed knee flexion and AP translations were also performed.

Overall, while IK results were adequate and consistent, instabilities emerged in subsequent analysis stages, particularly during the COMAK and ID steps. The resulting joint contact forces were unrealistically high and exhibited substantial noise, limiting their interpretability. An example of such outputs is presented in Figure A20. In addition, large reserve actuator forces and activations were observed at the TF and PF DoFs, indicating dynamic inconsistency in the simulations. Non-physiological patellar behaviour was consistently observed, particularly toward the end of the gait cycles, with excessive displacement and deviations from the femoral groove.

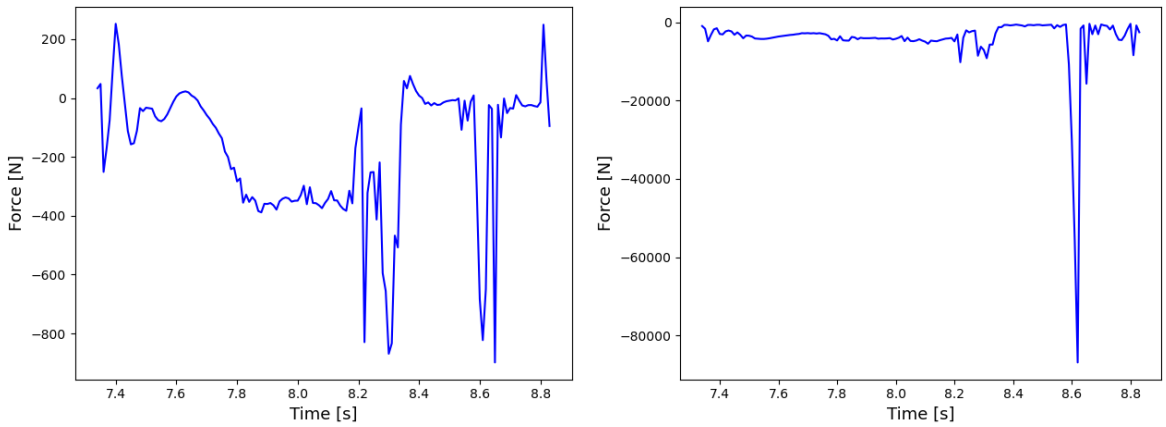

(**a**) (**b**)

Figure A20. Example of TF contact force components obtained from the COMAK analysis of a single gait cycle, showing high magnitudes and substantial noise. (**a**) Force component in the AP direction. (**b**) Force component in the SI direction (axial). The irregular behaviour indicates potential dynamic inconsistencies in the simulation.

To investigate the sources of these instabilities, additional simulation configurations were explored. COMAK solver parameters, including damping-related settings and allowable ranges for secondary kinematics, were adjusted in an attempt to improve numerical stability. Moreover, the experimental data from the CAMS-knee dataset were processed and filtered to assess whether signal noise contributed to the observed behaviour. The positioning of the implant components was also adjusted to evaluate the sensitivity of the simulations to implant alignment and try to improve estimates. All intermediate calculations and coordinate transformations were thoroughly reviewed to identify potential errors. However, none of these modifications led to measurable improvements in simulation outcomes.

Following these extensive troubleshooting efforts, additional baseline simulations were conducted using both the original TKA model configuration and the reference model used in Febrer-Nafría et al. (2023) [71], which was made available by one of the collaborators involved in this study. Nevertheless, these additional simulations did not resolve the previously observed instabilities.

Appendix J.6. Limitations and rationale for model transition

In light of all the efforts undertaken and the issues encountered, there are some limitations of the JAM modelling framework worth acknowledging. First, a considerable number of simulation frames failed to converge, indicating convergence issues within the COMAK optimisation process. When convergence is not achieved, COMAK propagates the solution from the previous time step [68], resulting in a model state that no longer satisfies dynamic equilibrium for the affected frame. Because each time step serves as the initial guess for the subsequent optimisation, these convergence failures accumulate and propagate over time, ultimately leading to erroneous estimates and numerical instability.

A second limitation is related to the high sensitivity of the model to implant component positioning. Joint contact forces are computed using an elastic foundation formulation, in which contact pressures depend on local surface penetration depth and elastic material properties. As a result, the contact response is numerically stiff and very sensitive to small variations in relative surface alignment, such that minor discrepancies in implant positioning can lead to large changes in contact forces and numerical instability. This sensitivity is further reinforced by the fact that implant positioning, although informed by subject-specific implantation data, relied partly on visual inspection in the absence of subject-specific bone geometries.

A third limitation concerns the substantial computational cost of this modelling approach. Even relatively simple walking simulations required several hours of computation on a high-performance computer, which significantly constrained the feasibility of iterative troubleshooting and systematic parameter exploration. Moreover, many studies employing this modelling framework rely on Monte Carlo–based sensitivity analyses to explore the solution space and identify robust parameter sets [69,71]. Implementing such approaches would require access to high-throughput computing resources, which were not available within the scope of this project.

Finally, the limited availability of documentation, examples, and community support for this specific modelling framework further restricted the ability to diagnose and resolve the observed issues. Despite repeated consultation with experts and multiple attempts to stabilise the simulations, the problems persisted. Given the remaining time constraints of the project and the absence of a clear resolution path, it was necessary to transition to an alternative modelling approach that offered greater numerical robustness while still enabling meaningful biomechanical analyses.

References

1. Arden, N.; Nevitt, M. Osteoarthritis: epidemiology. *Best Practice Research Clinical Rheumatology* **2006**, *20*, 3–25. https://doi.org/10.1016/j.berh.2005.09.007.
2. Bertozzi, L.; Stagni, R.; Fantozzi, S.; Cappello, A. *Biomechanical Modeling from In-Vivo Data*; Springer, 2008; pp. 133–160. https://doi.org/10.1007/978-3-540-89430-8\{_8.
3. Cui, A.; Li, H.; Wang, D.; Zhong, J.; Chen, Y.; Lu, H. Global, regional prevalence, incidence and risk factors of knee osteoarthritis in population-based studies. *EClinicalMedicine* **2020**, *29-30*, 100587. https://doi.org/10.1016/j.eclinm.2020.100587.
4. Qiao, L.; Li, M.; Deng, F.; Wen, X.; Deng, H.; Xue, Z.; Zhou, J.; Lin, J.; Amhare, A.F.; Xiang, R.; et al. Epidemiological trends of osteoarthritis at the global, regional, and national levels from 1990 to 2021 and projections to 2050. *Arthritis Research Therapy* **2025**, *27*, 199. https://doi.org/10.1186/s13075-025-03658-w.
5. Heidari, B. Knee osteoarthritis prevalence, risk factors, pathogenesis and features: Part I. *Caspian Journal of Internal Medicine* **2011**, *2*, 205–212.
6. Wieland, H.A.; Michaelis, M.; Kirschbaum, B.J.; Rudolphi, K.A. Osteoarthritis — an untreatable disease? *Nature Reviews Drug Discovery* **2005**, *4*, 331–344. https://doi.org/10.1038/nrd1693.
7. Mora, J.C.; Przkora, R.; Cruz-Almeida, Y. Knee osteoarthritis: pathophysiology and current treatment modalities. *Journal of Pain Research* **2018**, *Volume 11*, 2189–2196. https://doi.org/10.2147/jpr.s154002.
8. Griffin, T.M.; Guilak, F. The role of mechanical loading in the onset and progression of osteoarthritis. *Exercise and Sport Sciences Reviews* **2005**, *33*, 195–200. https://doi.org/10.1097/00003677-200510000-00008.
9. Andriacchi, T.P.; Koo, S.; Scanlan, S.F. GAIT mechanics influence healthy cartilage morphology and osteoarthritis of the knee. *Journal of Bone and Joint Surgery* **2009**, *91*, 95–101. https://doi.org/10.2106/jbjs.h.01408.
10. Gustafson, J.A.; Elias, J.J.; Fitzgerald, G.K.; Tashman, S.; Debski, R.E.; Farrokhi, S. Combining advanced computational and imaging techniques as a quantitative tool to estimate patellofemoral joint stress during downhill gait: A feasibility study. *Gait Posture* **2020**, *84*, 31–37. https://doi.org/10.1016/j.gaitpost.2020.11.016.
11. Jahn, J.; Ehlen, Q.T.; Huang, C.Y. Finding the Goldilocks Zone of Mechanical Loading: A Comprehensive review of mechanical loading in the prevention and treatment of knee osteoarthritis. *Bioengineering* **2024**, *11*, 110. https://doi.org/10.3390/bioengineering11020110.
12. Lee, R.; Kean, W.F. Obesity and knee osteoarthritis. *Inflammopharmacology* **2012**, *20*, 53–58. https://doi.org/10.1007/s10787-011-0118-0.
13. Heijink, A.; Gomoll, A.H.; Madry, H.; Drobnič, M.; Filardo, G.; Espregueira-Mendes, J.; Van Dijk, C.N. Biomechanical considerations in the pathogenesis of osteoarthritis of the knee. *Knee Surgery Sports Traumatology Arthroscopy* **2011**, *20*, 423–435. https://doi.org/10.1007/s00167-011-1818-0.
14. Liu, H.; Qin, L.; Liu, Y.; Meng, X.; Li, C.; He, M. Knee osteoarthritis rehabilitation: an integrated framework of exercise, nutrition, biomechanics, and physical therapist guidance—a narrative review. *European journal of medical research* **2025**, *30*, 826. https://doi.org/10.1186/s40001-025-03083-4.
15. Henak, C.R.; Anderson, A.E.; Weiss, J.A. Subject-Specific Analysis of joint contact mechanics: Application to the study of osteoarthritis and surgical planning. *Journal of Biomechanical Engineering* **2013**, *135*, 021003. https://doi.org/10.1115/1.4023386.
16. Stoddart, J.; Dandridge, O.; Garner, A.; Cobb, J.; Van Arkel, R. The compartmental distribution of knee osteoarthritis – a systematic review and meta-analysis. *Osteoarthritis and Cartilage* **2020**, *29*, 445–455. https://doi.org/10.1016/j.joca.2020.10.011.
17. Wei, J.; Gross, D.; Lane, N.; Lu, N.; Wang, M.; Zeng, C.; Yang, T.; Lei, G.; Choi, H.; Zhang, Y. Risk factor heterogeneity for medial and lateral compartment knee osteoarthritis: analysis of two prospective cohorts. *Osteoarthritis and Cartilage* **2018**, *27*, 603–610. https://doi.org/10.1016/j.joca.2018.12.013.
18. Mahmoudian, A.; Van Dieen, J.H.; Bruijn, S.M.; Baert, I.A.; Faber, G.S.; Luyten, F.P.; Verschueren, S.M. Varus thrust in women with early medial knee osteoarthritis and its relation with the external knee adduction moment. *Clinical Biomechanics* **2016**, *39*, 109–114. https://doi.org/10.1016/j.clinbiomech.2016.10.006.
19. Sharma, L. The role of knee alignment in disease progression and functional decline in knee osteoarthritis. *JAMA* **2001**, *286*, 188. https://doi.org/10.1001/jama.286.2.188.
20. Bergmann, G.; Graichen, F.; Rohlmann, A.; Westerhoff, P.; Heinlein, B.; Bender, A.; Ehrig, R. Design and calibration of load sensing orthopaedic implants. *Journal of Biomechanical Engineering* **2008**, *130*. https://doi.org/10.1115/1.2898831.

21. Komistek, R.D.; Kane, T.R.; Mahfouz, M.; Ochoa, J.A.; Dennis, D.A. Knee mechanics: a review of past and present techniques to determine in vivo loads. *Journal of Biomechanics* **2004**, *38*, 215–228. https://doi.org/10.1016/j.jbiomech.2004.02.041.
22. Markolf, K.L.; Gorek, J.F.; Kabo, J.M.; Shapiro, M.S. Direct measurement of resultant forces in the anterior cruciate ligament. An in vitro study performed with a new experimental technique. *Journal of Bone and Joint Surgery* **1990**, *72*, 557–567. https://doi.org/10.2106/00004623-199072040-00014.
23. Nisell, R. Mechanics of the knee. *Acta Orthopaedica Scandinavica* **1985**, *56*, 1–42. https://doi.org/10.3109/17453678509154159.
24. Wilson, D.R.; Walter, E.J.M.; Johnston, J.D. The measurement of joint mechanics and their role in osteoarthritis genesis and progression. *Medical Clinics of North America* **2008**, *93*, 67–82. https://doi.org/10.1016/j.mcna.2008.08.004.
25. Yang, Y.; Wang, Y.; Zheng, N.; Cheng, R.; Zou, D.; Zhao, J.; Tsai, T.Y. Development and validation of a novel in vitro joint testing system for reproduction of in vivo dynamic muscle force. *Bioengineering* **2023**, *10*, 1006. https://doi.org/10.3390/bioengineering10091006.
26. Bowd, J.; Van Rossom, S.; Williams, D.; Elson, D.; Wilson, C.; Whatling, G.; Holt, C.; Jonkers, I. Using musculoskeletal modelling to estimate knee joint loading pre and post high tibial osteotomy. *Clinical Biomechanics* **2022**, *101*, 105855. https://doi.org/10.1016/j.clinbiomech.2022.105855.
27. Wang, B.; Mao, Z.; Guo, J.; Yang, J.; Zhang, S. The non-invasive evaluation technique of patellofemoral joint stress: a systematic literature review. *Frontiers in Bioengineering and Biotechnology* **2023**, *11*, 1197014. https://doi.org/10.3389/fbioe.2023.1197014.
28. Andersen, M.S. *Introduction to musculoskeletal modelling*; Woodhead Publishing, 2020; pp. 41–80. https://doi.org/10.1016/b978-0-12-819531-4.00004-3.
29. Fernandez, J.W.; Akbarshahi, M.; Kim, H.J.; Pandy, M.G. Integrating modelling, motion capture and x-ray fluoroscopy to investigate patellofemoral function during dynamic activity. *Computer Methods in Biomechanics Biomedical Engineering* **2007**, *11*, 41–53. https://doi.org/10.1080/10255840701551046.
30. Ali, A.A.; Mannen, E.M.; Rullkoetter, P.J.; Shelburne, K.B. Validated computational framework for evaluation of in vivo knee mechanics. *Journal of Biomechanical Engineering* **2020**, *142*. https://doi.org/10.1115/1.4045906.
31. Abdullah, M.; Hulleck, A.A.; Katmah, R.; Khalaf, K.; El-Rich, M. Multibody dynamics-based musculoskeletal modeling for gait analysis: a systematic review. *Journal of NeuroEngineering and Rehabilitation* **2024**, *21*, 178. https://doi.org/10.1186/s12984-024-01458-y.
32. Ackland, D.C.; Keynejad, F.; Pandy, M.G. Future trends in the use of X-ray fluoroscopy for the measurement and modelling of joint motion. *Proceedings of the Institution of Mechanical Engineers Part H Journal of Engineering in Medicine* **2011**, *225*, 1136–1148. https://doi.org/10.1177/0954411911422840.
33. Akbarshahi, M.; Schache, A.G.; Fernandez, J.W.; Baker, R.; Banks, S.; Pandy, M.G. Non-invasive assessment of soft-tissue artifact and its effect on knee joint kinematics during functional activity. *Journal of Biomechanics* **2010**, *43*, 1292–1301. https://doi.org/10.1016/j.jbiomech.2010.01.002.
34. Fiorentino, N.M.; Atkins, P.R.; Kutschke, M.J.; Goebel, J.M.; Foreman, K.B.; Anderson, A.E. Soft tissue artifact causes significant errors in the calculation of joint angles and range of motion at the hip. *Gait Posture* **2017**, *55*, 184–190. https://doi.org/10.1016/j.gaitpost.2017.03.033.
35. Zheng, L.; Li, K.; Shetye, S.; Zhang, X. Integrating dynamic stereo-radiography and surface-based motion data for subject-specific musculoskeletal dynamic modeling. *Journal of Biomechanics* **2014**, *47*, 3217–3221. https://doi.org/10.1016/j.jbiomech.2014.08.009.
36. Monfrini, R.; Rossetto, G.; Scalona, E.; Galli, M.; Cimolin, V.; Lopomo, N.F. Technological Solutions for Human Movement Analysis in Obese Subjects: A Systematic review. *Sensors* **2023**, *23*, 3175. https://doi.org/10.3390/s23063175.
37. Rajagopal, A.; Dembia, C.L.; DeMers, M.S.; Delp, D.D.; Hicks, J.L.; Delp, S.L. Full-Body musculoskeletal model for Muscle-Driven simulation of human GaIT. *IEEE Transactions on Biomedical Engineering* **2016**, *63*, 2068–2079. https://doi.org/10.1109/tbme.2016.2586891.
38. Curreli, C.; Di Puccio, F.; Davico, G.; Modenese, L.; Viceconti, M. Using Musculoskeletal Models to Estimate in vivo Total Knee Replacement Kinematics and Loads: Effect of Differences Between Models. *Frontiers in Bioengineering and Biotechnology* **2021**, *9*, 703508. https://doi.org/10.3389/fbioe.2021.703508.
39. Dur, N.; Wesseling, M.; Macri, E.; Runhaar, J. Fluoroscopy: Taking a closer look at joint motion in osteoarthritis. *Osteoarthritis Imaging* **2024**, *4*, 100240. https://doi.org/10.1016/j.ostima.2024.100240.

40. Fregly, B.J.; Rahman, H.A.; Banks, S.A. Theoretical Accuracy of Model-Based Shape Matching for Measuring Natural Knee Kinematics with Single-Plane Fluoroscopy. *Journal of Biomechanical Engineering* **2005**, *127*, 692–699. https://doi.org/10.1115/1.1933949.
41. Li, G.; Van De Velde, S.K.; Bingham, J.T. Validation of a non-invasive fluoroscopic imaging technique for the measurement of dynamic knee joint motion. *Journal of Biomechanics* **2008**, *41*, 1616–1622. https://doi.org/10.1016/j.jbiomech.2008.01.034.
42. Ivester, J.C.; Cyr, A.J.; Harris, M.D.; Kulis, M.J.; Rullkoetter, P.J.; Shelburne, K.B. A reconfigurable High-Speed Stereo-Radiography system for Sub-Millimeter measurement of in vivo joint kinematics. *Journal of Medical Devices* **2015**, *9*. https://doi.org/10.1115/1.4030778.
43. Nasab, S.H.H.; Bänteli, P.; List, R. Using Video-Fluoroscopy and multibody modelling to unveil the influence of a gradually reducing femoral radius on ligament elongation patterns following posterior Cruciate-Retaining total Knee arthroplasty. *Applied Sciences* **2024**, *14*, 9910. https://doi.org/10.3390/app14219910.
44. Navacchia, A.; Kefala, V.; Shelburne, K.B. Dependence of muscle moment arms on in vivo Three-Dimensional kinematics of the knee. *Annals of Biomedical Engineering* **2016**, *45*, 789–798. https://doi.org/10.1007/s10439-016-1728-x.
45. Gerus, P.; Sartori, M.; Besier, T.F.; Fregly, B.J.; Delp, S.L.; Banks, S.A.; Pandy, M.G.; D'Lima, D.D.; Lloyd, D.G. Subject-specific knee joint geometry improves predictions of medial tibiofemoral contact forces. *Journal of Biomechanics* **2013**, *46*, 2778–2786. https://doi.org/10.1016/j.jbiomech.2013.09.005.
46. Walker, P.; Rovick, J.; Robertson, D. The effects of knee brace hinge design and placement on joint mechanics. *Journal of Biomechanics* **1988**, *21*, 965–974. https://doi.org/10.1016/0021-9290(88)90135-2.
47. Arnold, E.M.; Ward, S.R.; Lieber, R.L.; Delp, S.L. A model of the lower limb for analysis of human movement. *Annals of Biomedical Engineering* **2009**, *38*, 269–279. https://doi.org/10.1007/s10439-009-9852-5.
48. Taylor, W.R.; Schütz, P.; Bergmann, G.; List, R.; Postolka, B.; Hitz, M.; Dymke, J.; Damm, P.; Duda, G.; Gerber, H.; et al. A comprehensive assessment of the musculoskeletal system: The CAMS-Knee data set. *Journal of Biomechanics* **2017**, *65*, 32–39. https://doi.org/10.1016/j.jbiomech.2017.09.022.
49. Heinlein, B.; Graichen, F.; Bender, A.; Rohlmann, A.; Bergmann, G. Design, calibration and pre-clinical testing of an instrumented tibial tray. *Journal of Biomechanics* **2007**, *40*, S4–S10. https://doi.org/10.1016/j.jbiomech.2007.02.014.
50. List, R.; Postolka, B.; Schütz, P.; Hitz, M.; Schwilch, P.; Gerber, H.; Ferguson, S.J.; Taylor, W.R. A moving fluoroscope to capture tibiofemoral kinematics during complete cycles of free level and downhill walking as well as stair descent. *PLoS ONE* **2017**, *12*, e0185952. https://doi.org/10.1371/journal.pone.0185952.
51. Burckhardt, K.; Szekely, G.; Notzli, H.; Hodler, J.; Gerber, C. Submillimeter measurement of cup migration in clinical standard radiographs. *IEEE Transactions on Medical Imaging* **2005**, *24*, 676–688. https://doi.org/10.1109/tmi.2005.846849.
52. Nejad, Z.I.; Khalili, K.; Nasab, S.H.H.; Schütz, P.; Damm, P.; Trepczynski, A.; Taylor, W.R.; Smith, C.R. The capacity of generic musculoskeletal simulations to predict knee joint loading using the CAMS-Knee datasets. *Annals of Biomedical Engineering* **2020**, *48*, 1430–1440. https://doi.org/10.1007/s10439-020-02465-5.
53. Belli, I.; Joshi, S.; Prendergast, J.M.; Beck, I.; Della Santina, C.; Peternel, L.; Seth, A. Does enforcing glenohumeral joint stability matter? A new rapid muscle redundancy solver highlights the importance of non-superficial shoulder muscles. *PLoS ONE* **2023**, *18*, e0295003. https://doi.org/10.1371/journal.pone.0295003.
54. Kutzner, I.; Trepczynski, A.; Heller, M.O.; Bergmann, G. Knee Adduction Moment and Medial Contact Force – Facts about Their Correlation during Gait. *PLoS ONE* **2013**, *8*, e81036. https://doi.org/10.1371/journal.pone.0081036.
55. Halder, A.; Kutzner, I.; Graichen, F.; Heinlein, B.; Beier, A.; Bergmann, G. Influence of limb alignment on mediolateral loading in total knee replacement. *Journal of Bone and Joint Surgery* **2012**, *94*, 1023–1029. https://doi.org/10.2106/jbjs.k.00927.
56. Pataky, T.C. One-dimensional statistical parametric mapping in Python. *Computer Methods in Biomechanics Biomedical Engineering* **2011**, *15*, 295–301. https://doi.org/10.1080/10255842.2010.527837.
57. Hume, D.R.; Navacchia, A.; Ali, A.A.; Shelburne, K.B. The interaction of muscle moment arm, knee laxity, and torque in a multi-scale musculoskeletal model of the lower limb. *Journal of Biomechanics* **2018**, *76*, 173–180. https://doi.org/10.1016/j.jbiomech.2018.05.030.
58. Sritharan, P.; Lin, Y.; Pandy, M.G. Muscles that do not cross the knee contribute to the knee adduction moment and tibiofemoral compartment loading during gait. *Journal of Orthopaedic Research®* **2012**, *30*, 1586–1595. https://doi.org/10.1002/jor.22082.

59. Hume, D.R.; Kefala, V.; Harris, M.D.; Shelburne, K.B. Comparison of Marker-Based and stereo radiography knee kinematics in activities of daily living. *Annals of Biomedical Engineering* **2018**, *46*, 1806–1815. https://doi.org/10.1007/s10439-018-2068-9.
60. Reinschmidt, C.; Van Den Bogert, A.; Nigg, B.; Lundberg, A.; Murphy, N. Effect of skin movement on the analysis of skeletal knee joint motion during running. *Journal of Biomechanics* **1997**, *30*, 729–732. https://doi.org/10.1016/s0021-9290(97)00001-8.
61. Andriacchi, T.P.; Stanwyck, T.S.; Galante, J.O. Knee biomechanics and total knee replacement. *The Journal of Arthroplasty* **1986**, *1*, 211–219. https://doi.org/10.1016/s0883-5403(86)80033-x.
62. Tanifuji, O.; Sato, T.; Mochizuki, T.; Koga, Y.; Yamagiwa, H.; Endo, N.; Kobayashi, K.; Omori, G. Three-dimensional in vivo motion analysis of normal knees using single-plane fluoroscopy. *Journal of Orthopaedic Science* **2011**, *16*, 710–718. https://doi.org/10.1007/s00776-011-0149-9.
63. Garner, A.J.; Dandridge, O.W.; Amis, A.A.; Cobb, J.P.; Van Arkel, R.J. Partial and Combined Partial knee arthroplasty: Greater Anterior-Posterior stability than posterior Cruciate–Retaining total knee arthroplasty. *The Journal of Arthroplasty* **2021**, *36*, 3765–3772.e4. https://doi.org/10.1016/j.arth.2021.06.025.
64. Halewood, C.; Traynor, A.; Bellemans, J.; Victor, J.; Amis, A.A. Anteroposterior laxity after Bicruciate-Retaining total knee arthroplasty is closer to the native knee than ACL-Resecting TKA: a biomechanical cadaver study. *The Journal of Arthroplasty* **2015**, *30*, 2315–2319. https://doi.org/10.1016/j.arth.2015.06.021.
65. Lenhart, R.L.; Kaiser, J.; Smith, C.R.; Thelen, D.G. Prediction and validation of Load-Dependent behavior of the tibiofemoral and patellofemoral joints during movement. *Annals of Biomedical Engineering* **2015**, *43*, 2675–2685. https://doi.org/10.1007/s10439-015-1326-3.
66. Delp, S.; Loan, J.; Hoy, M.; Zajac, F.; Topp, E.; Rosen, J. An interactive graphics-based model of the lower extremity to study orthopaedic surgical procedures. *IEEE Transactions on Biomedical Engineering* **1990**, *37*, 757–767. https://doi.org/10.1109/10.102791.
67. Smith, C.R.; Vignos, M.F.; Lenhart, R.L.; Kaiser, J.; Thelen, D.G. The influence of component alignment and ligament properties on tibiofemoral contact forces in total knee replacement. *Journal of Biomechanical Engineering* **2016**, *138*, 021017. https://doi.org/10.1115/1.4032464.
68. Smith, C. GitHub - clnsmith/opensim-jam: An OpenSim Framework to Model and Simulate Articular Joint Mechanics, 2019.
69. Smith, C.R.; Brandon, S.C.; Thelen, D.G. Can altered neuromuscular coordination restore soft tissue loading patterns in anterior cruciate ligament and menisci deficient knees during walking? *Journal of Biomechanics* **2018**, *82*, 124–133. https://doi.org/10.1016/j.jbiomech.2018.10.008.
70. Van Rossom, S.; Wesseling, M.; Smith, C.R.; Thelen, D.G.; Vanwanseele, B.; Dieter, V.A.; Jonkers, I. The influence of knee joint geometry and alignment on the tibiofemoral load distribution: A computational study. *The Knee* **2019**, *26*, 813–823. https://doi.org/10.1016/j.knee.2019.06.002.
71. Febrer-Nafría, M.; Dreyer, M.J.; Maas, A.; Taylor, W.R.; Smith, C.R.; Nasab, S.H.H. Knee kinematics are primarily determined by implant alignment but knee kinetics are mainly influenced by muscle coordination strategy. *Journal of Biomechanics* **2023**, *161*, 111851. https://doi.org/10.1016/j.jbiomech.2023.111851.